BNL-113979-2017-JA

Connecting Structural and Transport Properties of Ionic Liquids with Cationic Oligoether Chains

S. I. Lall-Ramnarine, M. Zhao, C. Rodriguez, R. Fernandez, N. Zmich, E. D. Fernandez, S. B. Dhiman, E. W. Castner Jr., and J. F. Wishart

Submitted to Journal of the Electrochemical Society

May 2017

Chemistry Department

Brookhaven National Laboratory

U.S. Department of Energy
USDOE Office of Science (SC),
Basic Energy Sciences (BES) (SC-22)

DISCLAIMER

Connecting Structural and Transport Properties of Ionic Liquids with Cationic Oligoether Chains

Sharon I. Lall-Ramnarine,[z,a] Man Zhao,[b] Chanele Rodriguez,[a] Rahonel Fernandez,[a] Nicole Zmich,[a,c] Eddie D. Fernandez,[a] Surajdevprakash B. Dhiman,[c] Edward W. Castner Jr.,[z,b] and James F. Wishart[z,c]

[a] Department of Chemistry, Queensborough Community College of the City University of New York, Bayside, NY 11364, USA
[b] Department of Chemistry and Chemical Biology, Rutgers, The State University of New Jersey, Piscataway, NJ 08854, USA
[c] Chemistry Division, Brookhaven National Laboratory, Upton, NY 11973, USA
[z] Corresponding Authors: slallramnarine@qcc.cuny.edu; ed.castner@rutgers.edu; wishart@bnl.gov

X-ray diffraction and molecular dynamics simulations were used to probe the structures of two families of ionic liquids containing oligoether tails on the cations. Imidazolium and pyrrolidinium bis(trifluoromethylsulfonyl)amide ILs with side chains ranging from 4 to 10 atoms in length, including both linear alkyl and oligo-ethylene oxide tails, were prepared. Their physical properties, such as viscosity, conductivity and thermal profile, were measured and compared for systematic trends. Consistent with earlier literature, a single ether substituent substantially decreases the viscosity of pyrrolidinium and imidazolium ILs compared to their alkyl congeners. Remarkably, as the number of ether units in the pyrrolidinium ILs increases there is hardly any increase in the viscosity, in contrast to alkylpyrrolidinium ILs where the viscosity increases steadily with chain length. Viscosities of imidazolium ether ILs increase with chain length but always remain well below their alkyl congeners. To complement the experimentally determined properties, molecular dynamics simulations were run on the two ILs with the longest ether chains. The results point to specific aspects that could be useful for researchers designing ILs for specific applications.

Introduction

The focus of the ionic liquid (IL) community is shifting beyond the mere measurement of physical properties and identification of trends arising from particular structural moieties. Researchers are delving deeper into the nanostructural interactions between the ions to determine the topographical landscape of the ions within the liquids that influence IL properties.[1-3] Such information is valuable when tuning the properties of ILs for particular applications. The ability to tune the properties of ionic liquids for specific applications is a major factor in their allure as remarkable solvents that make it possible to do extreme chemistry without extreme conditions. It has been acknowledged that although ionic liquids have a combination of physical properties that make them attractive alternatives to traditional solvents, they have relatively high viscosities that

hamper their practical application in large-scale processes. For example, in the area of electrochemical energy storage devices there is still an urgent need for improved electrolytes exhibiting properties of combustion resistance, high conductivity, and wide electrochemical windows. ILs with improved transport properties (viscosity, conductivity and diffusivity) would be perfect candidates to address this need. Structural modification of the IL cation and anion is a proven tool to dramatically alter IL properties. In particular, substituting ether functionalities for alkyl functionalities on IL cations has been shown to reduce the viscosity of ionic liquids significantly.[2,4-6] In this work we examine the effect of incorporating oligoether side chains of varying lengths (1-3 repeating ethoxy units, Figure 1) on the physical properties and structural characteristics of imidazolium and pyrrolidinium NTf_2 ionic liquids in comparison to the homologous series bearing alkyl side chains.

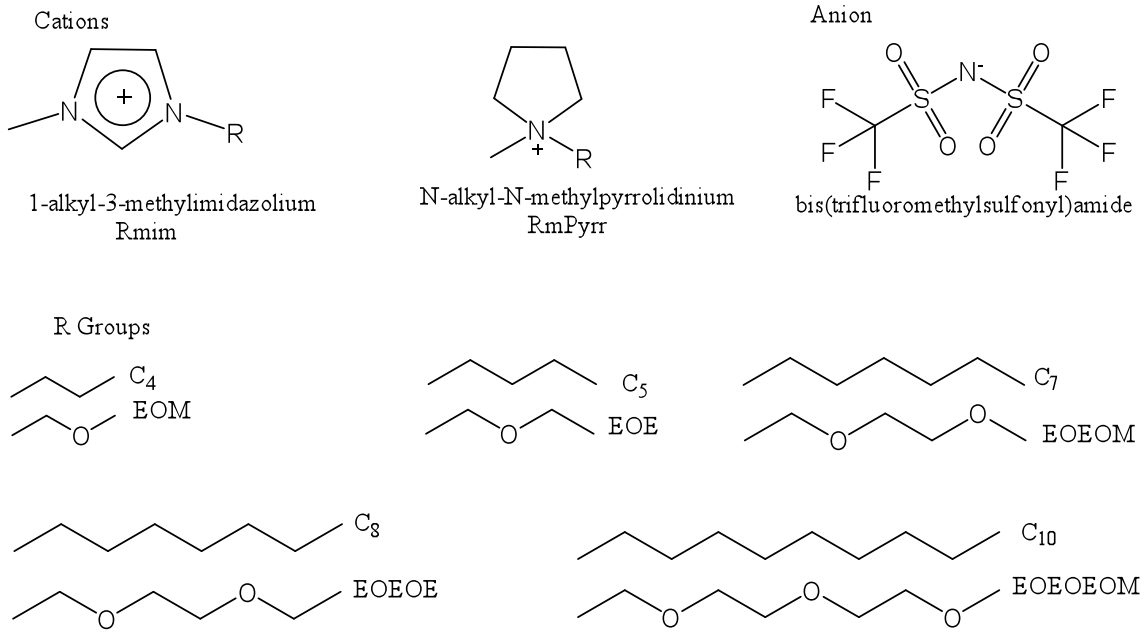

Figure 1. Structures of the ions used in this study. Chain lengths are 4, 5, 7, 8, and 10 atoms.

ILs with Ether Tails

Ether and polyether groups have been exploited for their liquefying and transport-improving properties for many years, including their incorporation into cations and anions to yield liquid ion conductive polymers.[7] In the 1980's Cooper and Angell proposed tetraalkylammonium salts containing methoxyethyl side chains as improved ambient temperature electrolytes for electrochemical devices owing to their reduced melting points and ability to dissolve high concentrations of lithium salts. They reported melting points of 158 ˚C for $BuNEtMe_2$ BF_4 and 13 ˚C for $MeO(CH_2)_2NEtMe_2$ BF_4.[8] The approach of substituting ether or polyether (polyethylene oxide, PEO or polyethylene glycol, PEG) side chains for alkyl side chains on IL cations and anions has become increasingly popular. Relative to alkyl-functionalized ILs, ether-functionalized ILs exhibit lower viscosities and melting points, higher conductivities and greater electrochemical stabilities, making them significantly more useful for practical applications. For example, the ionic liquid dimethylethylmethoxyethyl ammonium

bis(trifluoromethylsulfonyl)amide ($(CH_3OCH_2CH_2)N(CH_3)_2CH_2CH_3$ NTf_2) has a viscosity of 60 cP (25 ˚C), a conductivity of 3.1 mS cm^{-1} (25 ˚C), an electrochemical window of 5.48 V and a glass transition temperature of -96 ˚C.[9] There are numerous reports of ether functionalized ILs as electrolytes for lithium ion batteries,[10-13] in electrochemical double layer capacitors and in dye sensitized solar cells.[14,15] In many cases ether or polyether functionalities have been incorporated into IL cations to increase their affinity for CO_2 absorption,[16,17] SO_2 absorption,[18,19] extraction of metal ions such as Hg^{2+}, La^{3+},[20,21] dissolution of carbohydrates, glycolipids and glycoproteins[22-24] and for enzyme stabilization and activation.[12] The Pernak group has reported antimicrobial and antielectrostatic effects in alkoxymethyl substituted pyridinium and imidazolium cations with 10-14 carbon atoms in the alkoxy group.[25,26] Recently, Matsumoto et al. reported on the use of "oligomeric" (polyether) ILs for the preparation of graphene from graphite under microwave conditions. The graphene sheets showed negligible deterioration and were redispersible (up to 100 mg/mL) in the ILs.[27] The favorable properties exhibited by ether functionalized ILs over their alkyl counterparts, leading to such a wide range of applications, has prompted the exploration of their nanoscale structure in order to understand the origins of their desirable properties and how they can be further enhanced.

Molecular dynamics (MD) simulations suggest that there is reduced electrostatic interaction between cations and anions in ether functionalized ILs, due to the polar ether group, when compared to alkyl.[28] More recently, MD simulations and X-ray diffraction studies have shown that in cations with ether tails or side chains, the tails are curled towards the positive head of the cation or wrap the cation if long enough (Figure 2),[1,2,12,28] effectively reducing the coulombic interactions between the cations and anions. The anions adjoin both the polar ether sites as well as the positive site of the cation. This behavior suppresses the nanosegregation of polar and non-polar domains present in alkyl substituted ILs (where non-polar chains extend outwards from the cations) and results in significant differences in the physical properties of the ILs.

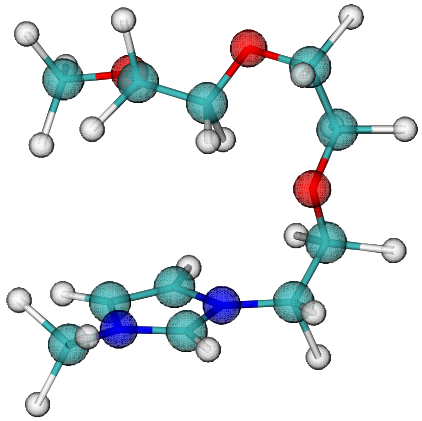

Figure 2. Example of ether tail curling in EOEOEOMmim NTf_2 in a representative structure generated by the TRAVIS program[29] from the MD simulations described in this paper. Note that it is the consensus of structures with very different ether chain orientations around the imidazolium ring, as will be described in the discussion.

Although numerous applications and physical properties of ether-functionalized ILs are reported, there are still gaps in the structure and physical property data sets for several ILs in this category. In light of this lack of information, the numerous advantages of ether

containing ILs and our interest in producing lower viscosity and higher conducting ILs, we undertook this study to systematically examine the effect of lengthening oligoether side chains on IL physical properties. We are ultimately interested in examining the nanoscale interactions between the ions that give rise to the physical properties, and for that reason we undertook molecular dynamics simulations on the ILs with the longest chain (the triether EOEOEOM) to complement previous simulations on imidazolium ILs containing the diether EOEOM chain.[28]

Results / Discussion

Thermal Properties and Densities.

The glass transition temperatures (T_g), melting points (T_m) and densities of the studied ILs are reported in Table 1. The T_g values for the pyrrolidinium ether ILs are the same or lower than those for the alkylpyrrolidinium ILs with the same number of atoms. For the imidazolium series the ether and alkyl T_g values are comparable for the short chains but the ethers are higher for the 8- and 10-atom chains. The T_g of EOEOEOMmim NTf_2 is 8 ˚C higher than all the other ILs studied, suggesting a higher degree of dynamic entanglement with the tri-ether chain and the H-bonding imidazolium cation.

TABLE I. Thermal properties and densities of NTf_2 ionic liquids.

Cation(s)	Glass Transition Point, T_g [a] ˚C	Melting Point, T_m [a] ˚C	Density at 22 ˚C g/mL
EOMmPyrr	-89	[b]	1.46@ 20°C
C_4mPyrr	-89	-7.6 [6]	1.39@ 23°C
EOEmPyrr	-91	[b]	1.41
C_5mPyrr	-86	7.6	1.36
EOEOMmPyrr	-90	[b]	1.39
C_7mPyrr	-85	18.4	1.30
EOEOEmPyrr	-88	[b]	1.35
C_8mPyrr	-83	-16	1.28
EOEOEOMmPyrr	-85	[b]	1.37
C_{10}mPyrr	-85 [c],[30]	9.5 [30]	1.25 [30]
EOMmim	-85	[b]	1.45
C_4mim	-87	-3	1.44
EOEmim	-86	-13	1.39
C_5mim	-85 [31]	-9 [31]	1.40 [31]
EOEOMmim	-84	[b]	1.44
C_7mim	-85	7	1.34
EOEOEmim	-83	14	1.41
C_8mim	-86	-23 [32]	1.28
EOEOEOMmim	-76	[b]	1.43
C_{10}mim	-83 [31]	-29 [31]	1.27 [31]

[a] All values are onset temperatures. [b] Not observed. [c] Reanalysis of original data from ref. [30], where the midpoint value of -82 ˚C was reported.

In eight of the ten ether ILs studied, the presence of the ether groups appears to inhibit crystallization to the extent that melting points could not be observed, including

all of the pyrrolidinium salts. In contrast, all ten ILs with alkyl side chains were observed to crystallize. This behavior is likely a result of the previously discussed attraction of the polar ether chain to the cation causing it to curl towards or wrap the cation, attenuating coulombic interactions between the ions and inhibiting crystallization (due to a higher degree of disorder) or reducing lattice energies. We investigate the structural consequences of ether chain curling below.

The densities of the ether-substituted ILs are almost always higher than those of the corresponding alkyl substituted ILs. The increase in mass from replacing a methylene group with an oxygen atom is trivial; the differences in density must arise from differences in the way the ions pack due to the way the ether tails change their interactions and the nanoscale structure of the IL. Overall, the densities of the ILs decrease as the length of the alkyl or ether chain increases, primarily due to the dilution of the denser NTf_2 anion as the volume fraction of the cation increases.

Viscosity and Conductivity.

Viscosities and conductivities for the twenty ionic liquids are presented in Table II, and the viscosities at 25˚C are depicted in Figure 3 as functions of total chain length.

TABLE II. Conductivities, viscosities and Walden products of NTf_2 ionic liquids at 25 ˚C and VTF fit parameters for the viscosities.

Cation	Conductivity mS/cm 25 ˚C	Viscosity cP [a] 25 ˚C	Walden Product $PScm^2/mol$	$\ln(\eta_0/cP)$ [b]	D	T_0, K
EOMmPyrr	3.9 [c]	54	0.62	-2.06 [d],33	5.59	155.1
C_4mPyrr	2.7 [c]	75	0.61	-2.28 [34]	6.11	154.8
EOEmPyrr	3.4 [c]	53	0.56	-2.09 [34]	5.59	155.1
C_5mPyrr	2.1 [c]	90	0.61	-2.34 [d],33	6.15	157.0
EOEOMmPyrr	2.4 [35]	55	0.45	-2.08	5.54	156.2
C_7mPyrr	0.8	127	0.36	-2.43	6.61	156.2
EOEOEmPyrr	2.0	56	0.40	-1.97	5.25	159.0
C_8mPyrr	1.1	140	0.58	-2.43	6.55	157.9
EOEOEOMmPyrr	1.5	64	0.36	-2.12	5.32	161.4
C_{10}mPyrr	0.69 [30]	150	0.42	-2.26 [30]	6.34	159.3
EOMmim	4.6	45	0.60	-1.95	4.74	163.7
C_4mim	3.3	50	0.48	-1.93 [d],36	4.99	160.8
EOEmim	3.3 [e],37	46	0.59[e]	-2.05	4.92	162.2
C_5mim	2.2 [31]	58	0.39	-2.13 [d],36	5.39	159.2
EOEOMmim	2.1	55	0.37	-2.14	5.06	163.6
C_7mim	1.27	80	0.35	-2.21 [d],36	5.72	159.6
EOEOEmim	1.78	61	0.37	-2.35	5.36	163.0
C_8mim	1.41	93	0.47	-2.44 [d],36	6.30	156.5
EOEOEOMmim	1.28	80	0.37	-2.22	4.87	171.6
C_{10}mim	0.55	119	0.26	-2.42 [d],36	6.29	159.1

[a] Calculated from the VTF parameters. [b] Citations in this column apply to all the VTF parameters. [c] Measured with the HP impedance analyzer. All others were measured with the YSI conductivity meter. [d] Fitted from data from the reference cited. [e] Measured or calculated at 20 ˚C.

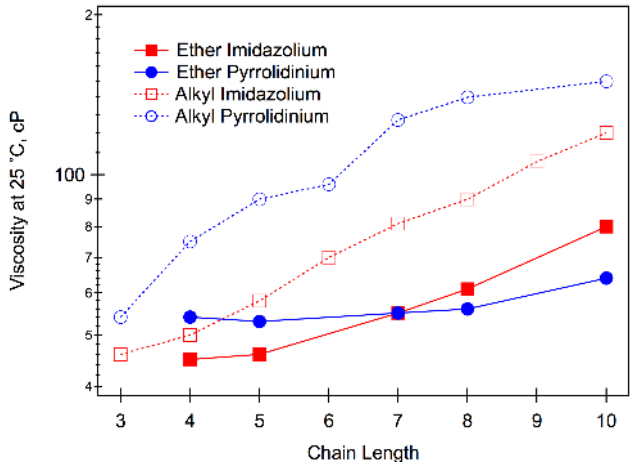

Figure 3. Viscosities of the imidazolium and pyrrolidinium ether and alkyl NTf_2 ionic liquids as calculated from VTF parameters at 25 ˚C, plotted against the total number of C and O atoms in the chain. Alkylimidazolium NTf_2 viscosities are from reference 36 and alkylpyrrolidinium NTf_2 viscosities for n = 3, 6 and 10 are from reference 30.

The effect of increasing alkyl chain length on viscosities within IL families has been well documented in the literature.[31] Viscosities increase with increasing alkyl chain length; at 25 ˚C they range from 75 cP for C_4mPyrr to 150 cP for C_{10}mPyrr and 51 cP for C_4mim NTf_2 to 120 cP for C_{10}mim NTf_2. Unlike the alkyl ILs, the pyrrolidinium ILs containing ether side chains show very little change in viscosity with increasing chain length (53-56 cP) until a modest increase to 64 cP for the 10-atom triether side chain. In the imidazolium series there is a more pronounced increase in viscosity with ether chain length, ranging from 45 cP for EOMmim NTf_2 to 80 cP for EOEOEOMmim NTf_2. This viscosity increase with ether chain length is roughly proportional to the alkyl case but the viscosities of the ether-substituted imidazolium salts are still much lower compared to their alkyl analogues.

These comments require some degree of caution since they are based on viscosities measured at a single temperature. We therefore collected temperature-dependent viscosity data for the ILs we prepared and analyzed it using the Vogel-Tammann-Fulcher relation, along with doing our own VTF analysis of literature viscosity data for the sake of consistency. With minor exceptions, both families of ether ILs have *higher* limiting viscosities (η_0) and critical temperatures (T_0) than their alkyl congeners, although the differences are small. More significantly, the D parameters of all of the ether ILs are smaller in magnitude than each of the corresponding alkyl ILs, most by substantial amounts. Angell has related the D parameter to the "fragility" of a wide variety of liquids and glasses.[38] Liquids having D parameters of smaller magnitude are more fragile, and their viscosities decrease more rapidly in a super-Arrhenius behavior as the temperature rises above T_g. Thus, all of the ether ILs are more fragile than their alkyl congeners, and the lower room-temperature viscosities observed for the ethers are consequences of their lower fragilities. The physical factors that determine fragility are the matter of significant investigation; these differences between ether and alkyl side chains are a part of that puzzle.

The conductivities of ILs listed in Table II generally decrease as the length of the alkyl chain increases. The Walden rule[38] states that the product of the molar conductivity and the viscosity should be constant for a particular fluid. Table II lists the Walden products for the 20 ionic liquids. There is no consistent trend in comparing the Walden products for corresponding ether and alkyl congeners among either IL cation family. However it is noted that the Walden products, which can be interpreted as a measure of conductivity corrected for molarity and viscosity, drop off with increasing chain length (with the exception of the octyl chain in both cases). Walden products are often used to quantify "ionicity",[38] or the degree to which the constituent anions and cations can diffuse independently to carry current. It is clear that the motion of oppositely charged ions becomes more correlated as the side chains lengthen, resulting in lower effective conductivity.

X-ray scattering results

Transport properties of ionic liquids are intimately linked to their nanoscale structure, and previous structural and molecular dynamics studies of imidazolium, ammonium and phosphonium ILs with pendant ether groups[1,2,28,39-41] have shown that their organization on the molecular scale is different than their normal alkyl chain congeners. While alkyl chains tend to exist in extended conformations with mostly *trans* dihedral angles, ether chains have a large fraction of *gauche* conformations, particularly across C-C bonds connected to ether oxygens.[1,2,28,39] The *gauche* conformations cause the ether tails to curl around the cations and remain adjacent to the polar, ionic domain of the IL rather than extend to form a separate nonpolar domain, as alkyl chains do when they get long enough.[2,42-44]

Nanosegregation of the nonpolar domains in alkyl chain ILs has been documented in numerous X-ray scattering experiments[45-49] that have been extensively dissected by theoretical treatments.[44,50-53] In ILs containing relatively dense anions that provide contrast for X-ray scattering,[54] nanoscale segregation of nonpolar domains is manifested by the appearance of a peak (often called a first sharp diffraction peak or "pre-peak" in the literature) in the X-ray scattering structure function $S(q)$ at a low q value in the range from 0.25-0.5 $Å^{-1}$), which increases in intensity and shifts to lower q as the alkyl chain lengthens. Existing X-ray scattering results for ether ILs[1,2,40,41] show no evidence of a pre-peak, consistent with their tendency to curl rather than extend into separate domains.

We undertook X-ray scattering measurements and MD simulations on the ILs reported here because our set of imidazolium ether ILs extends to longer chain lengths than had been previously studied (to date only MOMmim NTf_2 and MOEOMmim NTf_2)[1,40,41] and there had been no experimental or theoretical studies on the pyrrolidinium ether NTf_2 congeners. Figures 4 and 5 depict X-ray scattering structure functions for the sets of ether and alkyl-functionalized imidazolium and pyrrolidinium ILs, respectively. Dealing with the imidazolium set first, our data is consistent with earlier X-ray and MD results.[44-46] For the alkylimidazolium ILs, the pre-peak starts as a shoulder for C_5mim NTf_2 and develops into a resolved peak that shifts to lower q as the alkyl chain extends from octyl to decyl. Among the ether imidazolium ILs, there is no evidence for a pre-peak except for a weak, broad shoulder in the case of EOEOEmim NTf_2, and no pre-peak is evident even for the longer-chain EOEOEOMmim NTf_2. This is also consistent with previous X-ray results on ether ILs. [2,40,41]

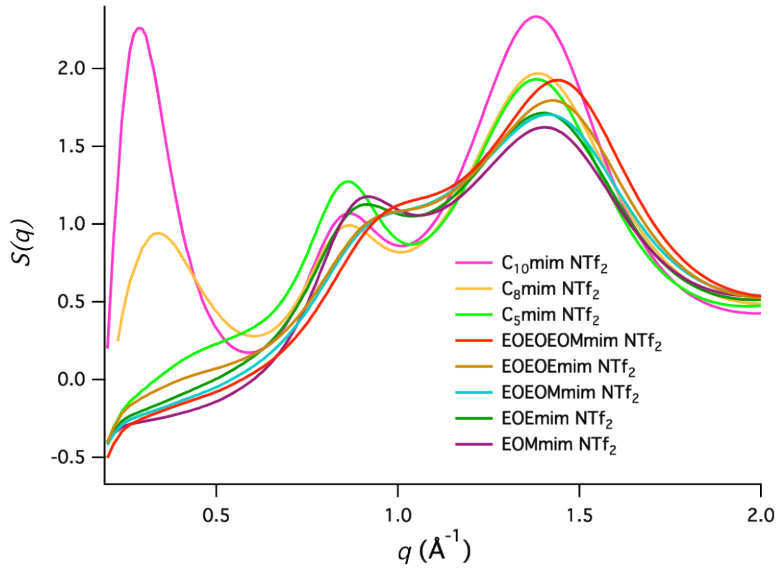

Figure 4. Experimental X-ray scattering structure functions for the imidazolium ILs.

Shimizu et al.[1] have observed that "the suppression of the pre-peak in the ether-substituted ILs is not caused by structural changes in the polar network but rather by the (re-)organization around it of the non-polar domains." We agree completely with this statement but it is also clear from our scattering data that the polar network is increasingly perturbed as the ether side chains get longer. The other peaks in the structure functions for the alkyl imidazolium ILs represent the charge alternation between anions and cations ($q \sim 0.86$ Å^{-1}) and the adjacency of the anions and cations ($q \sim 1.4$ Å^{-1}). While the amplitudes of these two peaks change with alkyl chain length, their positions do not vary much. However, in the ether imidazolium case the charge alternation peak gets broader as the ether chain lengthens and it shifts to higher q. The adjacency peak also shifts to higher q as the ether chain lengthens. Because the observed experimental structure factors are actually the sums of large, phase-staggered scattering terms that mostly cancel each other[52,53] it is easy to over-interpret such peak shifts, but it is clear that the curling of the ether cation tails is having an effect on the polar network structure. The nature of this effect is more easily interpreted through MD simulations, as discussed below and in the literature.[1,28]

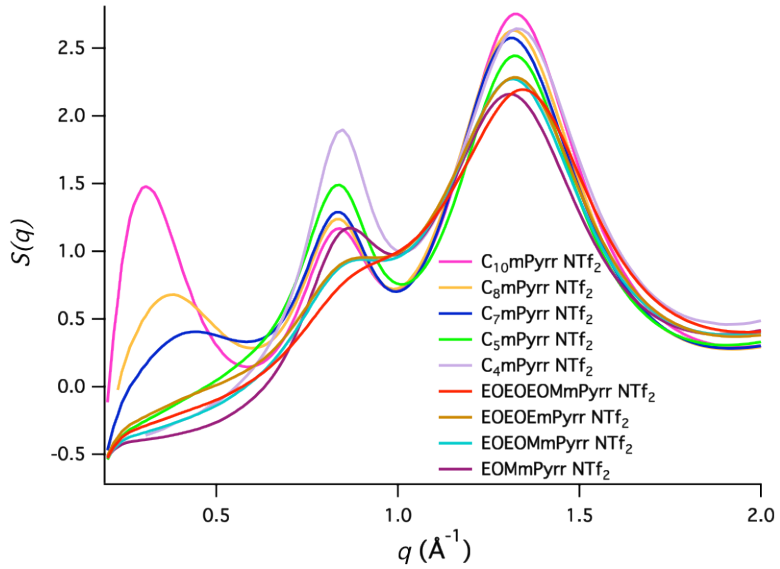

Figure 5. Experimental X-ray scattering structure functions for the pyrrolidinium ILs. Data for C_nmPyrr NTf_2 is from refs. 47 and 49.

The experimental X-ray scattering structure functions for the pyrrolidinium ILs (Figure 5) tell largely the same story as the imidazolium ones, with a minor variation when it comes to the adjacency peak. The pre-peak is evident for the heptyl, octyl and decyl ILs but not for the pentyl one. In the pyrrolidinium NTf_2 series the pre-peak appears between pentyl and hexyl,[49] perhaps due to the fact that the volume of the pyrrolidinium cation head is about 11 cm^3/mol larger than that of the imidazolium one, which happens to be the rough equivalent of one methylene group.[55] Just as in the imidazolium case, there are no pre-peaks for the ether pyrrolidinium ILs (again the 8-member ether EOEOEmPyrr NTf_2 bucks the trend slightly) and the charge alternation peaks shift to higher q as they broaden out with chain length. The ether pyrrolidinium adjacency peaks shift slightly to higher q but remain in the same range as the corresponding alkyl ones while their amplitudes vary non-monotonically with chain length. Thus, the polar network in pyrrolidinium ILs is also altered by the ether chains but in a different way that may reflect on the differences in transport properties between longer-chain pyrrolidinium and imidazolium ILs.

Molecular dynamics simulations

As discussed above, a number of MD simulations have investigated the structure of alkyl[1,2,28,43,44] and ether[1,28] imidazolium NTf_2 ILs, and alkylpyrrolidinium NTf_2 ILs.[49] Since those results were well established, we concentrated on simulating the ILs in our set with the longest ether chains, EOEOEOMmim NTf_2 and EOEOEOMmPyrr NTf_2.

Total structure factors $S(q)$ and their partitioning into components

The liquid structure functions $S(q)$ obtained from the X-ray scattering experiments and MD simulations on EOEOEOMmim NTf_2 and EOEOEOMmPyrr NTf_2 are compared in Figure 6. As expected from previous results on NTf_2-anion ILs,[56] the part of $S(q)$ for $q > 2.0$ Å^{-1} results from intramolecular contributions, while intermolecular interactions contribute to $S(q)$ for $q < 2.0$ Å^{-1}. As noted above, unlike the $S(q)$ functions for ILs with alkyl chains of $n \geq 6$, no pre-peak is observed in the range of $0.25 < q < 0.50$ Å^{-1} in the X-

ray experimental data for the oligoethers. However, small shoulders in the simulated $S(q)$ are observed for EOEOEOMmim NTf_2.

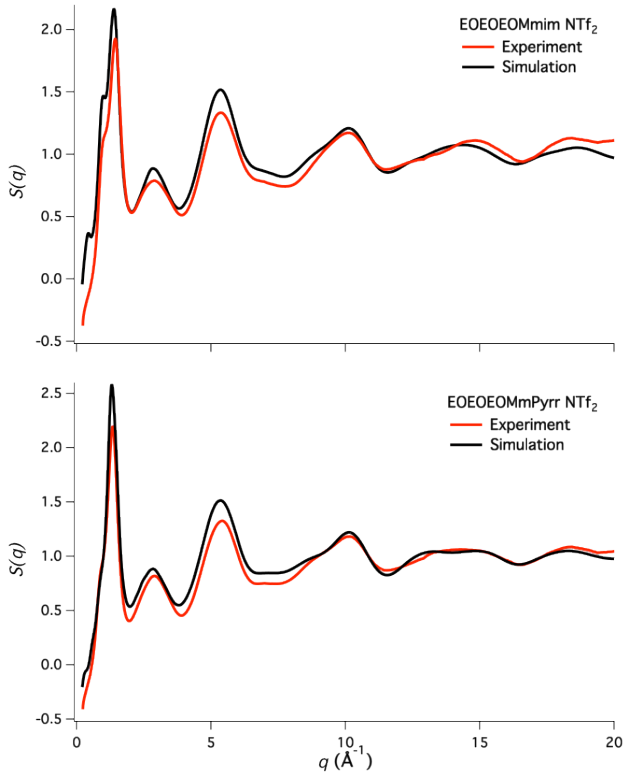

Figure 6. Comparisons of the liquid structure functions $S(q)$ for the EOEOEOMmim NTf_2 and EOEOEOMmPyrr NTf_2 ILs obtained from high-energy X-ray scattering experiments (red) at APS beamline 11-ID-C and from MD simulations (black).

As we have shown previously,[2,49,53,56-58] understanding the intermediate-range order contributions to the IL structure can best be understood by partitioning the $S(q)$ obtained from molecular simulations. Figure 7 shows the ionic partitioning, where the total $S(q)$ is considered as the sum of structural correlations between ions as follows:[53,56]

$$S(q) = S_{\text{anion-anion}}(q) + S_{\text{anion-cation}}(q) + S_{\text{cation-anion}}(q) + S_{\text{cation-cation}}(q) \quad (1)$$

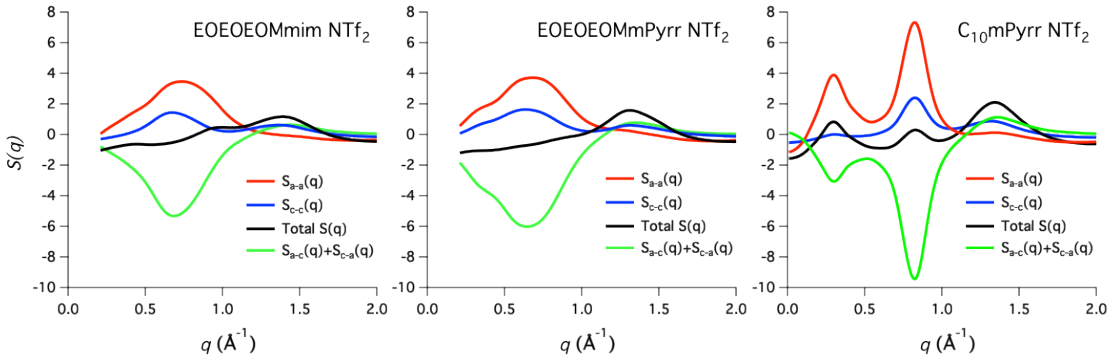

Figure 7. Ionic partitioning of the simulated structure factors $S(q)$ (black) for EOEOEOMmim NTf_2, EOEOEOMmPyrr NTf_2 and C_{10}mPyrr NTf_2 into anion-anion

(red), cation-cation (blue) and anion-cation/cation-anion (green) contributions. Data for C_{10}mPyrr NTf_2 is from ref. 49.

At first glance the partitioned $S(q)$ contributions for EOEOEOMmim NTf_2 and EOEOEOMmPyrr NTf_2 in Figure 7 appear very similar in shape, with a slight difference below q = 0.4 Å^{-1}. Minor variations in the destructive interference between the positive contributions from anion-anion and cation-cation correlations, offset by the negative contributions of the anion-cation/cation-anion correlations, give rise to the features seen in the observed total $S(q)$. However, the effects of oligoether substitution on the structure of the ILs only become clear when comparison is made with the partitioned structure factors of a corresponding alkyl IL, C_{10}mPyrr NTf_2, shown on the right side of Figure 7. The partitioned adjacency peaks (q ~ 1.3-1.4 Å^{-1}) in the ether and alkyl ILs are qualitatively similar, but there are enormous differences between the ether and alkyl cases for the charge alternation (q ~ 0.8-0.9 Å^{-1}) and polar-nonpolar domain alternation (pre-peak, q < 0.5 Å^{-1}) regions. For C_{10}mPyrr NTf_2, all of the ionic correlations show narrow, well-resolved and strong peaks and anti-peaks in q-space, indicating a high degree of nanostructural organization. The opposite is true for the oligoethers, where there are only single, broad peaks in each of the ionic correlations over the range 0.3 < q < 1.0 Å^{-1}. The broad peaks in the ether cases are shifted to lower q compared to the charge alternation peaks in C_{10}mPyrr NTf_2, indicating an increase in spacing within the polar network due to the curling of the ether tails around and among the ions.

The effect of ether tail curling into the polar network is also apparent when the partial $S(q)$ for cation-cation correlation is further decomposed into correlations for the positively-charged cation head groups and ether tails as shown in Figure 8. In C_{10}mPyrr NTf_2 we observe that there is a strong self-correlation for the cation heads in the charge alternation region, which is the indicator for the local structure of the polar network, and another one in the polarity alternation region. When the decyl group is replaced by the oligoether in EOEOEOMmPyrr NTf_2, the head-head correlation peak in the charge alternation region shifts to lower q, suggesting an increase in spacing between cation heads as the ether tails curl around them. EOEOEOMmim NTf_2 shows the same behavior.

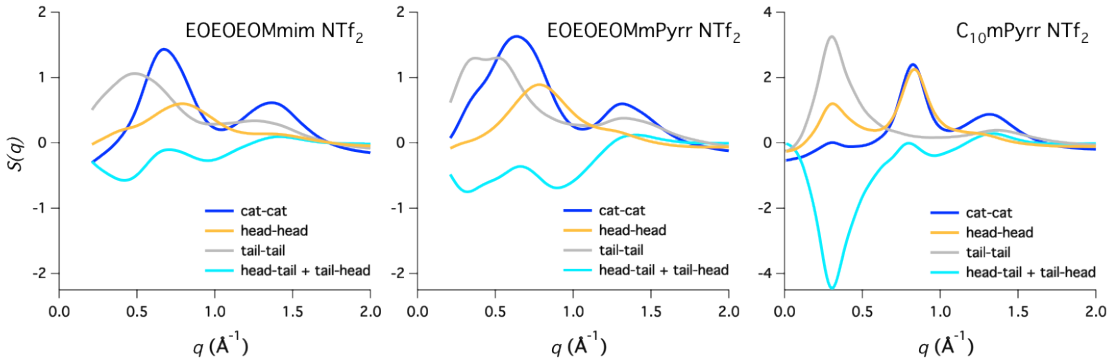

Figure 8. Partitioning of the simulated structure factor $S(q)$ into correlations between the cation head, cation tail and anion moieties for EOEOEOMmim NTf_2, EOEOEOMmPyrr NTf_2 and C_{10}mPyrr NTf_2. For clarity, the vertical scales for the ether ILs are expanded by a factor of 2. Data for C_{10}mPyrr NTf_2 is from refs. 47 and 49.

In the analysis of the experimental scattering $S(q)$ above we noted that there were shifts and changes in the charge alternation peaks for both families of ILs as the length of

the ether chain increased, indicating a disruption of the polar network. However the nature of the disruption is obscured in the total $S(q)$ due to the effects of massive cancellations among the ionic scattering terms. Fortunately, the MD simulations allow us to visualize the discrete effects by dissecting the total structure function into meaningful correlation-based components.

Simulation boxes

Snapshots of the equilibrated simulation boxes for EOEOEOMmPyrr NTf_2 and EOEOEOMmim NTf_2 are shown in Figure 10. The color scheme is given in Figure 9: red NTf_2 anions, blue cationic head groups (including the *N*-methyl and *N*-methylene groups), and grey EOEOEOM cation tails. Note that it is easy to observe aggregation of the charged red anionic and blue cationic head-group moieties, as spatially distinct from the grey EOEOEOM tails.

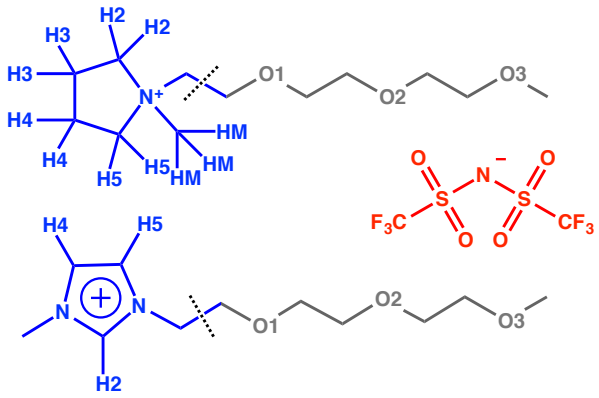

Figure 9. Color scheme for Figure 10 and labeling scheme for Figures 11 and 12. The labeling scheme follows the precedent of Smith et al.[28]

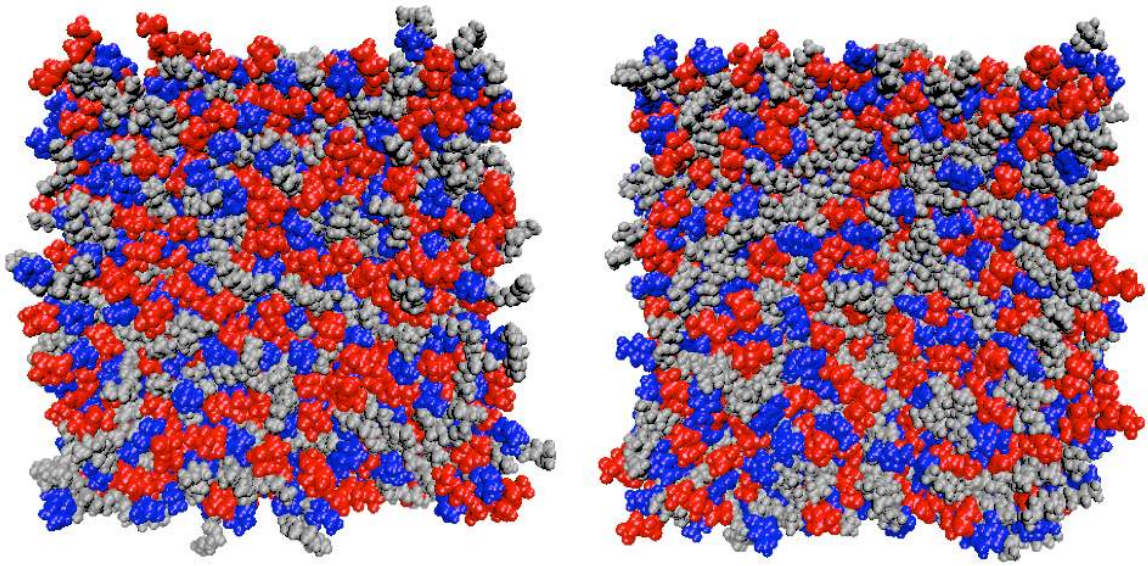

Figure 10. Sub-ionic partitioning of the equilibrated simulation boxes for EOEOEOMmPyrr NTf_2 (left) and EOEOEOMmim NTf_2 (right). The dimensions of the two boxes are 8.54 and 8.66 nm, respectively, on each side. The color scheme is explained in Figure 9.

As in ILs with long alkyl tails,[1,42,44,45,59] the ether chains do have their own network of connectivity. While the ether chains are more polar than alkyl analogues, they still induce a degree of local nanophase segregation, an effect that has also been observed for more strongly polar alkylsilyl and alkylsiloxy tails on the same cations.[57,58] In the case of the ethers, however, this segregation is incomplete and disordered, as shown by the partitioned structure factors discussed above. Instead of a distinct peak in the polarity alternation region, as observed around q = 0.3 in C_{10}mPyrr NTf_2 (Figure 8), the inter-ionic correlations in Figure 7 drop off in that region, reflecting the incomplete segregation. Further understanding of the local environment can be obtained by studying selected radial distribution functions to identify specific structural interactions among the components of the ILs.

Structure of EOEOEOMmim NTf_2: Radial distribution functions

At the outset of the discussion of radial distribution functions (RDFs) it is important to make a distinction between the elegant simulation treatment of Shimizu et al.[1] based on the X-ray data of Russina and Triolo,[40,41] where the ether groups are connected by a methylene (CH_2) group between the imidazolium nitrogen and the first ether oxygen, and our ionic liquids where an ethylene (CH_2CH_2) group connects the cation nitrogen and the first ether oxygen. This difference is key because the extra CH_2 group enables enough conformational freedom for the first ether oxygen on the chain (labeled O1 in Figure 9) to interact closely with the nearest hydrogens of the cation head group to form a 6-member ring (counting from the H2 or H5 atom to O1). Such a configuration is shown in Figure 11. This sort of intramolecular interaction from the first oxygen to the imidazolium ring is sterically precluded for the shorter methylene-linked ether ILs such as MOMmim NTf_2 and MOEOMmim NTf_2 as the oxygen atoms cannot approach the imidazolium ring (envision the second carbon of the ether chain in Figure 11 as an oxygen).[1,40,41] Smith et al.[28] performed MD simulations on two of the shorter ethylene-linked ether ILs in our set (EOMmim NTf_2 and EOEOMmim NTf_2 as well as the corresponding BF_4^- salts) and they observed strong intramolecular correlations between O1 and the ring protons, while the correlations for O2 were primarily intermolecular. In their ethylene-linked imidazolium oligoether ILs, they found that the nearest ether oxygen (O1) is most likely to interact with the protons on the imidazolium ring, while Shimizu et al.[1] found that the terminal oxygen is the most likely to interact in the methylene-linked oligoether ILs.

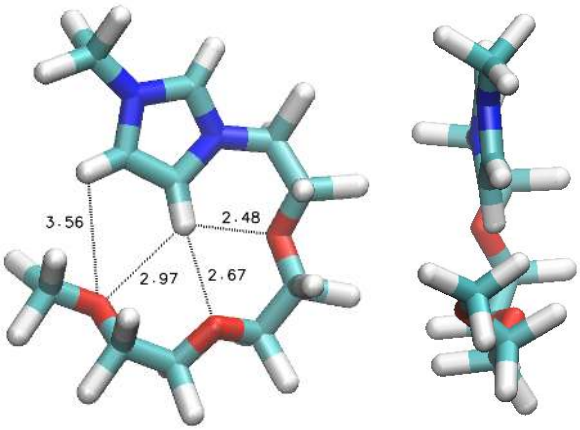

Figure 11. Two views of the structure of an EOEOEOMmim$^+$ cation selected from our MD simulation showing the ether chain conformation close to the plane of the imidazolium ring. Distances between atoms are given in Ångstroms.

Figure 12 presents the RDFs between the imidazolium ring hydrogen atoms and the ether and anion oxygen atoms that were calculated from our MD simulation of EOEOEOMmim NTf_2. The RDFs are also partitioned into intramolecular and intermolecular components, depending on whether the ether oxygen atom interacting with a particular proton is part of the same cation or not. All the graphs are presented on the same vertical scale so that the relative magnitudes of the distributions can be appreciated. They show that the first ether oxygen O1 has a very high probability of being in the vicinity of the H5 proton and a high probability of being near H2. O1 has a very low probability of being located near the H4 proton on the far side of the ring from the ether group's point of attachment. Figure 12 shows that this interaction is intermolecular (for obvious steric reasons), and would require the unlikely very close approach of two cations. The middle oxygen in the ether chain, O2, has lower probabilities of interaction with the ring hydrogens but they still rank in the same order, H5 > H2 > H4. The terminal oxygen O3 has the highest probability of interacting with H4 among all the ether oxygens. Our partitioned radial distribution functions are in accord with the partitioned analysis of Smith et al.[28] for the shorter ethylene-linked ether chains, although they did not distinguish between H4 and H5. The partitioned RDFs indicate that the interactions of O1 with H2 and H5 are almost exclusively intramolecular (even more so than for H2 in EOEOMmim NTf_2 [28]) and those for O2 are predominantly intramolecular. The interactions of O3 are mostly intermolecular, although weaker (longer) intramolecular interactions exist with H4 and H5.

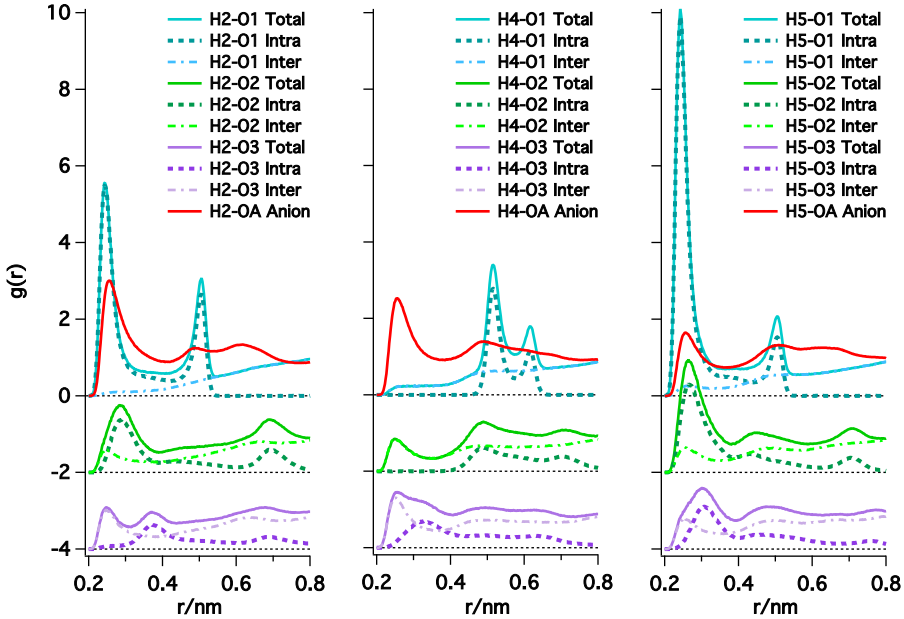

Figure 12. Radial distribution functions among the hydrogen atoms on the cation ring in EOEOEOMmim NTf_2 and the oxygen atoms in the oligoether and anion moieties. The labels are explained in Figure 9. The total RDFs for each interaction are partitioned into intramolecular and intermolecular correlations. Note that the four oxygen atoms of the anion are labeled together as OA. For clarity, the RDFs for O2 and O3 are offset by -2 and -4 units, respectively.

The RDFs indicate that association of the oxygens (OA) of the NTf_2^- anion with the ring hydrogens is strongest for H2, which is more acidic than H4 and H5. Despite the fact that H4 and H5 have essentially the same acidity, the anion oxygens associate more with H4 than H5. This is likely due to the competition from the intramolecular O2 oxygen for the H5 site and the lack of such competition for the H4 site.

The hydrogen-oxygen radial distribution functions for EOEOEOMmim NTf_2 point to a large extent of interactions between the ether tails and the imidazolium head groups that disrupt the structure of the polar network, as noted in the discussions of the experimental and calculated structure factors. Yet, the analysis of the methylene-linked imidazolium ether ILs (MOMmim NTf_2, MOEOMmim NTf_2 and MOEOEOMmim NTf_2) by Shimizu et al.[1] described a situation where the curling ether tails form a thin sheath around the polar network of the IL but do not disrupt it. The pattern in radial distribution functions between our work and theirs is consistent for the most distant oxygens (O8 in their case (Figure 8 of reference 1) and O3 in our case, which would be O9 if we used their nomenclature), but it is radically different for the nearest oxygens. The structural, dynamical and transport consequences of this minor modification in side chain structure merit further investigation.

Structure of EOEOEOMmim NTf_2: Spatial distribution functions (SDFs)

The strong intramolecular correlations observed in the RDFs between O1 and O2 on one hand and H5 and H2 on the other raise the question of whether they are due to energetically favorable interactions such as hydrogen bonding and dipole-dipole interactions or if they are simply due to adjacency enforced by bond connectivity. To shed light on this question we generated functions for the intramolecular spatial distribution of each of the ether oxygens around the imidazolium ring to which they are attached. The SDFs are depicted in Figure 13.

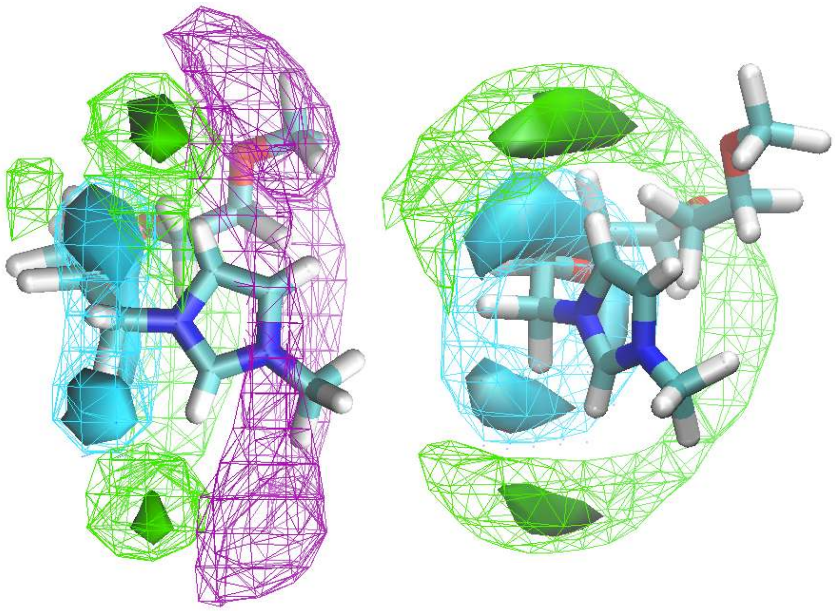

Figure 13. Two views of the intramolecular spatial distribution functions for the ether chain oxygen atoms in EOEOEOMmim NTf_2. The isosurface densities are given in units of nm^{-3}. The SDFs for O1 are depicted in cyan at densities of 5 (wireframe) and 20 (solid), those for O2 are depicted in green at densities of 3 (wireframe) and 15 (solid), and that

for O3 is depicted in purple at a density of 1.5. The O3 SDF was omitted from the oblique view on the right for clarity. The EOEOEOMmim$^+$ cation depicted is the representative structure shown in Figure 2.

It should be noted that the "representative" structure shown here and in Figure 2 with the ether chain hovering over the ring is the consensus of all the structures in the simulation, which have a wide range of different ether chain orientations. This has a tendency to average out the extremes of having the ether chains close to the plane of the ring (such as Figure 11), despite the higher probability of those configurations.

The SDF for O1 shows that the highest probability density occurs in regions close to the H2 and H5 hydrogens and in the imidazolium ring plane, although the O1 atom is free to rotate in a torus centered on the alpha carbon as shown by the cyan wireframe isosurface at 5 nm^{-3}. When located in the ring plane, O1 approaches H2 and H5 at distances of 0.24 to 0.25 nm in the 6-member configuration mentioned above but it cannot form what is considered to be a classical hydrogen bond with either of them. One operative definition of hydrogen bonding is an inter-heavy atom (in this case C2 or C5 to O1) distance less than 0.35 nm and a deviation from linearity of the C-H-O1 angle of 30˚ or less (i.e. bond angle $\geq$ 150˚).[60] While the distance criterion is met in the cases of C2-O1 and C5-O1 in our simulations, the angle distributions for both sites are sharply peaked around 110˚. The prevalence of these in-plane configurations could be attributed to a favorable dipole interaction but they could also be reinforced by the tendency of O2 to form classical, linear hydrogen bonds with H2 and H5 as shown by the solid green isosurfaces in Figure 13.

A lingering question is whether these strong intramolecular spatial correlations for O1 and O2 are a product of the particulars of the simulation or if they can be found and quantified by some experimental technique. We note that in support of their MD simulations that are consistent with our calculated RDFs, Smith, et al.[28] performed quantum chemistry calculations on the EOMmim$^+$ cation and found that the lowest energy configurations place O1 near H2 and H5 with distances of 0.242 and 0.244 nm, respectively. We also note that the intramolecular O1-H2 and O1-H5 correlations can be overcome by intermolecular forces in some situations. The crystal structures of EOMmim iodide, EOEOMmim iodide, and EOEOMmim bromide published by Fei, et al.[39] have O1-H2,H5 distances between 0.30 and 0.41 nm. More rigorous investigation is warranted, perhaps in the form of *ab initio* MD simulations. Labeled magnetic resonance techniques may permit experimental verification of this correlation, no matter what the cause.

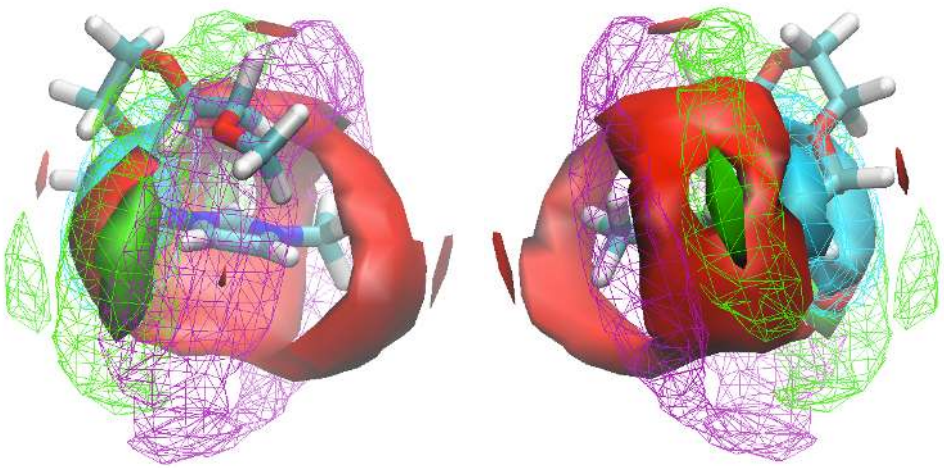

Figure 14. Two views of the aggregate SDF of the four oxygen atoms of the NTf_2^- anion (solid red isosurface at a density of 4 nm^{-3}), separated by 180˚ rotation around the vertical axis. The intramolecular O1, O2 and O3 SDFs and the cation are depicted as in Figure 13.

The aggregate spatial distribution of the four oxygen atoms of the NTf_2^- anion are shown in Figure 14. The intramolecular O1, O2 and O3 SDFs are also shown to indicate the spatial variation of the most common interactions. The observed SDF of the anion oxygens and its relation to the cation tail oxygen RDFs bear out the inferences drawn from the RDFs about the relative competing interactions and also suggest that H-bonding between H2 and NTf_2^- may often be bidentate (see the right side of Figure 14).

Structure of EOEOEOMmPyrr NTf_2: Radial and spatial distribution functions

We calculated the corresponding H-O radial distribution functions (Figure 15) and spatial distribution functions (Figure 16) for EOEOEOMmPyrr NTf_2 to compare with the imidazolium system, since the protons on alpha carbons bonded to the nitrogen center are only very weakly acidic. We were a bit surprised to find that the O1 ether oxygens have a very high probability of association with the methyl protons (HM) but no higher probability of associating with the proximal ring methylene protons H2 and H5 than does the terminal ether oxygen O3, despite the same degree of adjacency. However, the methyl protons are free to rotate around the methyl carbon to optimize their interaction with O1 while the methylene protons cannot, explaining the predominance of this interaction. Interactions of O2 with HM (at slightly longer distances) are equal parts intramolecular and intermolecular, while those with the ring protons H2 and H5 are mostly intermolecular. Interactions of O3 with the methyl and proximal methylene protons are equally probable, and more probable than those for O2. For all the ring protons (H2, H3, H4 and H5) the nearest neighbors were most likely to be NTf_2^- anions.

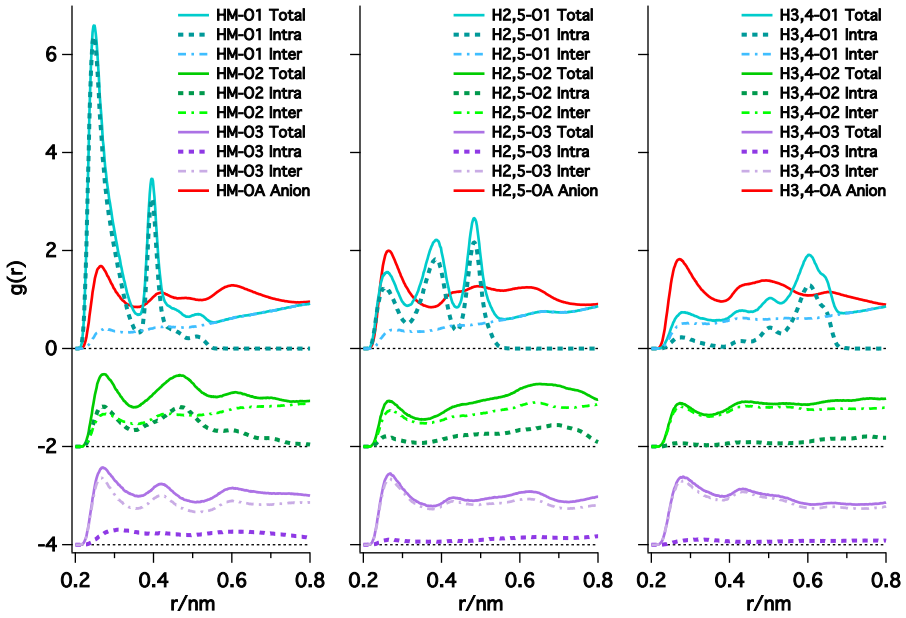

Figure 15. Radial distribution functions among hydrogen atoms on the cationic head group in EOEOEOMmPyrr NTf_2 and the oxygen atoms in the oligoether and anion moieties. The labels are explained in Figure 9. The total RDFs for each interaction are partitioned into intramolecular and intermolecular correlations. Note that the four oxygen atoms of the anion are labeled together as OA. For clarity, the RDFs for O2 and O3 are offset by -2 and -4 units, respectively.

We observe in Figure 16 that the intramolecular HM-O1 interaction causes the oligoether chain to persist in the quadrant of space close to the methyl group, partially shielding it from the anion oxygens. This tendency may influence the intermolecular forces responsible for mediating diffusion and viscosity in ways that could be related to the very weak increases in viscosity with increasing chain length observed in this system. As in the imidazolium case, it would be interesting to examine the structural consequences of using methylene-bridged ether groups, in particular in terms of the possibility of interaction with the methyl group and the consequences for diffusivity and viscosity.

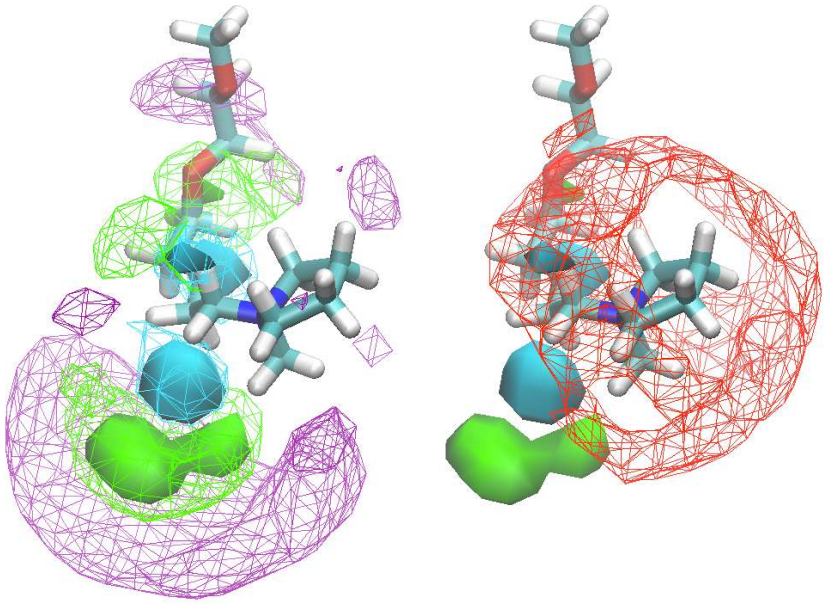

Figure 16. Intramolecular spatial distribution functions for the ether chain and anion oxygen atoms in EOEOEOMmPyrr NTf_2. The isosurface densities and colors are the same as in Figures 12 and 13. Two depictions from identical orientations are presented for clarity, with the (red) anion distribution omitted from the left picture and the lower-density ether oxygen isosurfaces omitted from the right picture. The $EOEOEOMmPyrr^+$ cation depicted is the representative structure generated by the TRAVIS program.[29]

Conclusion

Although the consequences of ether-functionality substitutions on the physical and structural properties of ionic liquids have been the objects of study for many years, this investigation has broken new ground in terms of fully characterizing the physical properties of longer oligoether ILs in both the imidazolium and pyrrolidinium families, and in X-ray scattering and molecular dynamics studies of oligoether pyrrolidinium ILs. We also broadened the set of oligoether imidazolium ILs that have been studied by X-ray scattering and extended the analysis of the MD simulations with interesting findings.

Our first significant observation was the extremely weak dependence of viscosity with increasing chain length in the oligoether pyrrolidinium NTf_2 series, even when compared to the corresponding imidazolium ILs. One of our motivations for the structural and MD studies was to find an underlying structural cause for this difference between the two cation types. Our structural studies have found that they have much in common on the large scale. X-ray scattering data shows that the polar networks of both IL families become increasingly disrupted as the oligoether chains get longer. We obtained multiple lines of evidence pointing to ether chain curling and disruptive interaction with the polar parts of the IL, particularly the cations. Zaitsau et al.[61] have found that this disruption weakens the polar network interactions in EOMmim NTf_2, EOEOMmim NTf_2 and EOEOEOMmim NTf_2 enough to reduce their enthalpies of vaporization by about 10 kJ/mol compared to their alkyl congeners. The weakened polar network interactions, combined with less segregation of the cation side chains, improve

the mobility of the ions in the ether ILs and reduces their viscosities compared to the alkyl cases.

We suspected that we might see specific interactions between the imidazolium cation heads and their oligoether tails that would provide a mechanism for such disruption of the polar network. Notably, an important fraction of these specific interactions are intramolecular and operate via the first and second oxygens in the ether chain, through favorable interactions in the case of O1 and hydrogen bonds in the case of O2. This happened to be the case because our ether chains are linked by ethylene groups that provide the conformational flexibility for the first oxygen to closely approach the H2 and H5 protons of the imidazolium ring, and also likely provide an optimal configuration for H-bonding of O2 with the same protons. Other groups[1,40,41] have done X-ray scattering and MD simulations on imidazolium ILs with methylene-linked oligoether tails that are sterically restricted from having such intramolecular interactions involving the first oxygen, and simulations showed that their structures are different on the molecular scale. Shimizu et al.[1] compared the methylene-linked imidazolium ether cations to scorpions because they curl their tails above their bodies. We think an apt comparison for the ethylene-linked imidazolium ether cations would be with lizards, since some species can curl their tails from side-to-side. It remains to be seen whether such distinctions lead to exploitable differences in structural, physical or dynamical properties between methylene- and ethylene-linked ether ILs.

Experimental

Materials. All chemicals and reagents were obtained from Sigma Aldrich and used without further purification, except for lithium bis(trifluoromethylsulfonyl)amide, which was obtained from IoLiTec, and 2-(methoxyethoxyethoxy)ethylbromide (BrEOEOEOM), which was purchased from TCI America. ^{1}H and ^{13}C NMR spectra were recorded on a Bruker 400 MHz NMR spectrometer. The water content measurements were performed using a Mettler Toledo DL39 Karl Fischer Coulometer.

Synthesis.

1a. Synthesis of *N*-(2-methoxyethyl)-*N*-methylpyrrolidinium bromide (EOMmPyrr Br)
N-methylpyrrolidine (5.00 g, 0.059 mol) was reacted with one equivalent of 2-bromoethylmethyl ether (8.20 g, 0.059 mol) in a round bottom flask with 40 mL of acetonitrile. The reaction was set up in an ice bath and allowed to warm to room temperature. It was left to stir for 4 days. The resulting product, an orange viscous liquid was purified by a two solvent recrystallization with hot acetonitrile and cold ethyl acetate, respectively. The recrystallized product was then vacuum filtered and washed with 20 mL of diethyl ether in a moisture-free tent. The product was rotary evaporated to remove residual solvent. The resulting compound was an orange solid (12.29 g, 93%, $C_8H_{18}NOBr$, Molar mass: 224.17 g/mol). ^{1}H(400 MHz; DMSO) δ 3.74-3.75(t, 2H), 3.56-3.59 (t, 2H), 3.48-3.50 (t, 4H), 3.30 (s, 3H), 3.03 (s, 3H), 2.07 (s, 4H); ^{13}C(101 MHz; D_2O) δ 66.50, 64.58, 62.44, 58.63, 48.50, 21.35.

2a. Synthesis of *N*-(2-ethoxyethyl)-*N*-methylpyrrolidinium bromide (EOEmPyrr Br)
N-methylpyrrolidine (5.00 g, 0.059 mol) was reacted with one equivalent of 2-bromoethylethylether (8.98 g, 0.0587 mol) in a round bottom flask with 20 mL of

acetonitrile. The reaction mixture was left to stir in an ice bath for 12 hours, then at room temperature for one day. The resulting product, an orange viscous liquid was purified by a two solvent recrystallization with hot acetonitrile and cold ethyl acetate, respectively. The recrystallized product was then vacuum filtered and washed with 20 mL of diethylether in a moisture-free tent. The product was rotary evaporated to remove residual solvent. The resulting compound was a pale yellow solid (10.62 g, 76%, $C_9H_{20}NOBr$, Molar mass: 238.20 g/mol). ^{1}H(400 MHz; D_2O) δ 3.80-3.81 (t, 2H), 3.40-3.51 (m, 8H), 2.96-2.98 (s, 3H), 1.04-1.09 (t, 3H).

3a. Synthesis of *N*-methyl-*N*-2-(2-methoxyethoxy)ethylpyrrolidinium bromide (EOEOMmpyrr Br)

N-methylpyrrolidine (4.14 g, 0.049 mol) was reacted with 1-bromo-2-(2-methoxyethoxy) ethane (9.35 g, 0.051 mol, 3% excess) in a round bottom flask with 25 mL of acetonitrile. The reaction mixture was set up in an ice bath, then left to stir at room temperature for 6 days. The dark brown, viscous liquid was purified by washing with ethyl acetate. The product was rotary evaporated to remove residual solvent. The resulting compound was a dark brown liquid (13.14 g, 94%, $C_{10}H_{22}NO_2Br$, Molar mass: 268.23 g/mol). ^{1}H(400 MHz; D_2O) δ 3.99-4.00 (t, 2H), 3.72-3.75 (m, 2H), 3.63-3.69 (m, 2H), 3.59-3.62 (q, 6H), 3.41 (s, 3H), 3.13 (s, 3H), 2.24-2.26 (d, 4H); ^{13}C(101 MHz; D_2O) δ 70.94, 69.48, 65.22, 64.70, 62.85, 58.03, 48.46, 21.04.

4a. Synthesis of *N*-(2-(2-ethoxyethoxy)ethyl)-*N*-methylpyrrolidinium bromide (EOEOEmPyrr Br)

N-methylpyrrolidine (5.00 g, 0.059 mol) was reacted with one equivalent of 2-(2-ethoxyethoxy)ethyl bromide (11.63 g, 0.059 mol) in a round bottom flask with 40 mL of acetonitrile. The reaction mixture was left to stir in an ice bath, then at room temperature for a week. The pale yellow liquid was purified by washing with ethyl acetate. The product was rotary evaporated to remove residual solvent. The resulting compound was a pale yellow liquid (14.65 g, 88%, $C_{11}H_{24}NO_2Br$, Molar mass: 282.26 g/mol). ^{1}H(400 MHz; D_2O) δ 3.99-4.00 (t, 2H), 3.71-3.75 (q, 4H), 3.60-3.62 (m, 8H), 3.14 (s, 3H), 2.25-2.27 (d, 4H), 1.20-1.24 (t, 3H); ^{13}C(101 MHz; D_2O) δ 70.20, 69.37, 67.14, 65.79, 65.23, 63.41, 49.05, 21.61, 14.64.

5a. Synthesis of *N*-methyl-*N*-(2-(2-(2-methoxyethoxy)ethoxy)ethyl)pyrrolidinium bromide (EOEOEOMmpyrr Br)

N-methylpyrrolidine (5.13 g, 0.0602 mol) was reacted with one equivalent of 1-(2-bromoethoxy)-2-(2-methoxyethoxy)ethane (13.67 g, 0.0602 mol) in a round bottom flask with 50 mL of acetonitrile. The reaction mixture was set up in an ice bath and left to stir at room temperature for 3 days. The product was purified by washing with ethyl acetate, then rotary evaporated to remove residual solvent. The resulting compound was a pale yellow liquid (17.81 g, 95%, $C_{12}H_{27}NO_3Br$, Molar mass: 312.3 g/mol). ^{1}H(400 MHz; D_2O) δ 3.99-4.00 (t, 2H), 3.70-3.74 (m, 4H), 3.59-3.66 (m, 10H), 3.40 (s, 3H), 3.13 (s, 3H), 2.24-2.25 (d, 4H); ^{13}C(101 MHz; D_2O) δ 70.99, 69.58, 69.47, 69.39, 65.23, 64.67, 62.87, 58.01, 48.41, 21.03.

6a. Synthesis of *N*-methyl-*N*-pentylpyrrolidinium bromide (C_5mPyrr Br)

N-methylpyrrolidine (5.00 g, 0.059 mol) was reacted with one equivalent of 1-bromopentane (8.91 g, 0.059 mol) in a round bottom flask with 40 mL of acetonitrile. The reaction mixture was set up in an ice bath, then left to stir at room temperature for 5

days. The pale yellow liquid was purified by washing with ethyl acetate. The product was rotary evaporated to remove residual solvent. The resulting compound was a clumpy pale yellow solid (12.84 g, 92%, $C_{10}H_{22}NBr$, Molar mass: 236.23 g/mol). ^{1}H(400 MHz; D_2O) δ 3.51-3.53 (t, 4H), 3.31-3.36 (m, 2H), 3.05 (s, 3H), 2.22 (s, 4H), 1.78-1.86 (m, 2H), 1.36-1.39 (q, 4H), 0.90-0.94 (t, 3H). ^{13}C(101 MHz; D_2O) δ 64.21, 22.70, 21.46, 21.26, 12.98.

7a. Synthesis of *N*-heptyl *N*-methylpyrrolidinium bromide (C_7mPyrr Br)

N-methylpyrrolidine (5.00 g, 0.059 mol) was reacted with one equivalent of 1-bromoheptane (10.57 g, 0.0587 mol) in a round bottom flask with 50 mL of acetonitrile. The reaction mixture was set up in an ice bath, then left to stir at room temperature for 12 days. The cloudy yellow liquid was purified by washing with ethyl acetate, and then rotary evaporated to remove residual solvent. The resulting compound was a cloudy viscous yellow liquid (13.04 g, 84%, $C_{12}H_{26}NBr$, Molar mass: 264.29 g/mol). ^{1}H(400 MHz; DMSO) δ 3.42-3.46 (t, 4H), 3.27-3.30 (t, 2H), 2.98 (s, 3H), 2.07 (s, 4H), 1.69 (s, 2H), 1.28-1.30 (m, 8H), 0.86-0.89 (t, 3H); ^{13}C(101 MHz; D_2O) δ 118.04, 63.36, 31.00, 28.16, 25.86, 22.91, 21.98, 21.06, 13.89, 1.14.

8a. Synthesis of *N*-methyl-*N*-octylpyrrolidinium bromide (C_8mPyrr Br)

N-methylpyrrolidine (5.00 g, 0.0587 mol) was reacted with one equivalent of 1-bromooctane (11.34 g, 0.0587 mol) in a round bottom flask with 20 mL of acetonitrile. The reaction mixture was left to stir at room temperature for 2 days. The brown, rock-like solid product was purified by washing with ethyl acetate, and then rotary evaporated to remove residual solvent. The resulting compound was a brown solid (14.74 g, 90%, $C_{13}H_{28}NBr$, Molar mass: 278.32 g/mol). ^{1}H(400 MHz; D_2O) δ 3.49-3.53 (m, 4H), 3.31-3.35 (m, 2H), 3.05 (s, 3H), 2.22 (s, 4H), 1.80-1.83 (t, 2H), 1.31-1.38 (m, 10H), 0.87-0.89 (t, 3H); ^{13}C (101 MHz; D_2O) δ 64.15, 30.92, 28.07, 21.93, 21.26, 13.33.

9a. Synthesis of *N*-methyl-*N*-decylpyrrolidinium bromide (C_{10}mPyrr Br)

N-methylpyrrolidine (10 g, 0.117 mol) dissolved in 25 mL of acetonitrile was reacted with one equivalent of 1-bromodecane (25.98 g, 0.117 mol) dissolved in 25 mL of acetonitrile in a round bottom flask. The reaction mixture was set up in an ice bath then left to stir at room temperature for 7 days. The yellow sludge was purified by washing with ethyl acetate, and then rotary evaporated to remove residual solvent. The resulting compound was a yellow solid (29.64 g, 83%, $C_{15}H_{32}NBr$, Molar mass 306.33 g/mol). ^{1}H(400 MHz; DMSO-d_6) δ 0.83-0.87 (s, 3H), 1.25 (s, 14H), 1.67-1.68 (m, 2H), 2.07 (s, 4H), 2.96 (s, 3H), 3.24-3.29 (m, 2H), 3.40-3.44 (m, 4H); ^{13}C (101 MHz; DMSO-d_6) δ 14.37, 21.52, 22.55, 23.37, 26.37, 28.96, 29.11, 29.26, 29.35, 31.74, 47.92, 63.66, 63.85.

10a. Synthesis of 1-butyl-3-methylimidazolium bromide (C_4mim Br)

1-methylimidazole (5.05 g, 0.0615 mol) dissolved in 15 mL of acetonitrile in a round bottom flask fitted with a stir bar and reflux condenser was reacted with one equivalent of 1-bromobutane (8.43 g, 0.0615 mol) dissolved in 15 mL of acetonitrile. The reaction mixture was left to stir at 50 °C for 4 days. The product was washed with 200 mL (10 x 20 mL) of ethyl acetate, rotary evaporated and dried in a high vacuum oven. The resulting product was a pale yellow liquid (11.18 g, 83%, $C_8H_{15}N_2Br$, Molar mass: 219.14 g/mol), ^{1}H (400 MHz; D_2O) δ 0.85-0.89 (t, 3H), 1.22-1.32 (m, 2H), 1.76-1.85 (m, 2H), 3.85 (s, 3H), 7.39 (d, 1H), 7.44-7.45 (d, 1H); ^{13}C (101 MHz; D2O) δ 12.7, 18.6, 31.3. 35.8, 49.3, 122.4, 127.5, 135.6

11a. Synthesis of 1-methyl-3-pentylimidazolium bromide (C_5mim Br)

1-methylimidazole (5.05 g, 0.0615 mol) dissolved in 15 mL of acetonitrile in a round bottom flask fitted with a stir bar and reflux condenser was reacted with one equivalent of 1-bromopentane (9.32 g, 0.0617 mol) dissolved in 15 mL of acetonitrile. The reaction mixture was left to stir for 7 days at 60 °C. The resulting product was washed with 100 mL (10 x 10 mL) of ethyl acetate. The final product was a clear, colorless liquid (12.66 g, 89%, $C_9H_{20}N_2Br$, Molar mass 233.16 g/mol). ^{1}H (400 MHz; D_2O) δ 0.75-0.79 (t, 3H), 1.17-1.24 (m, 4H), 1.75-1.81 (m, 2H), 3.80 (s, 3H), 4.08-4.11 (t, 2H), 7.33-7.34 (d, 1H), 7.38 (d, 1H) ^{13}C (101 MHz; D_2O) δ 12.2, 20.4, 27.9, 34.7, 48.6, 121.2, 122.4, 134.6.

12a. Synthesis of 1-heptyl-3-methylimidazolium bromide (C_7mim Br)

1-methylimidazole (5.06 g, 0.0616 mol) dissolved in 15 mL of acetonitrile in a round bottom flask fitted with a stir bar and reflux condenser was reacted with one equivalent of 1-bromoheptane (11.03 g, 0.0616 mol) dissolved in 15 mL of acetonitrile. The reaction was left to stir for 4 days at 55 °C. The resulting compound was then washed with 100 mL (10 x 10 mL) of ethyl acetate. The final product was a clear, colorless liquid (14.15 g, 88%, $C_{11}H_{24}N_2Br$, Molar mass 261.22 g/mol). ^{1}H (400 MHz; DMSO-d_6) δ 0.87 (t, 3H), 1.01-1.04 (m, 2H), 1.13-1.26 (m, 6H), 1.73-1.81 (m, 2H), 3.88 (s, 3H), 4.17-4.21 (t, 2H), 7.78 (d, 1H), 7.86 (d, 1H), 9.36 (s, 1H) ^{13}C (101 MHz; DMSO-d_6) δ 14.3, 21.2, 25.9, 28.5, 29.9, 31.5, 36.2, 49.2, 122.7, 123.9, 137.0.

13a. Synthesis of 1-methyl-3-octylimidazolium bromide (C_8mim Br)

1-methylimidazole (5.01 g, 0.0610 mol) dissolved in 15 mL of acetonitrile in a round bottom flask fitted with a stir bar and reflux condenser was reacted with one equivalent of 1-bromooctane (11.78 g, 0.0610 mol) dissolved in 15 mL of acetonitrile. The reaction mixture was left to stir for 6 days at 65 °C. The resulting compound was washed with 200 mL (10 x 20 mL) of ethyl acetate. The final product was a clear, colorless liquid (14.05 g, 84%, $C_{12}H_{26}N_2Br$, Molar mass 275.24 g/mol). ^{1}H (400 MHz; DMSO-d_6) δ 0.87 (t, 3H), 1.01-1.04 (m, 2H), 1.13-1.26 (m, 6H), 1.73-1.81 (m, 2H), 1.84-1.87 (m, 2H), 3.88 (s, 3H), 4.17-4.21 (t, 2H), 7.78 (d, 1H), 7.86 (d, 1H), 9.36 (s, 1H) ^{13}C (101 MHz; DMSO-d_6) δ 14.3, 21.2, 25.9, 28.5, 27.6, 29.9, 31.5, 36.2, 49.2, 122.7, 123.9, 137.0.

14a. Synthesis of 1-decyl-3-methylimidazolium bromide (C_{10}mim Br)

1-methylimidazole (5.0 g, 0.0609 mol) dissolved in 15 mL of acetonitrile in a round bottom flask fitted with a stir bar and reflux condenser was reacted with one equivalent of 1-bromodecane (12.73 mL, 0.0615 mol) dissolved in 15 mL of acetonitrile. The reaction mixture was heated at 65 °C and left to stir for 5 days. The reaction mixture was then rotary evaporated and the product was dried under high vacuum at room temperature to yield a colorless liquid (15.02 g, 81%, $C_{14}H_{30}N_2Br$, Molar mass 303.29 g/mol). ^{1}H (400 MHz; DMSO-d_6) δ 0.83-0.86 (t, 3H), 1.24 (s, 14H), 3.85 (s, 3H), 4.14-4.17 (t, 2H), 7.71 (d, 1H), 7.78 (d, 1H), 9.18 (s, 1H) ^{13}C (101 MHz; DMSO-d_6) δ 13.9, 22.0, 25.4, 28.3, 28.6, 28.7, 28.9, 29.4, 31.2, 35.7, 48.7, 122.2, 123.5, 136.5.

15a. Synthesis of 1-(2-methoxyethyl)-3-methylimidazolium bromide (EOMmim Br)

1-methylimidazole (5.12 g, 0.0624 mol) dissolved in 15 mL of acetonitrile was reacted with one equivalent of 2-bromoethylmethylether (8.67 g, 0.0624 mol) dissolved in 15 mL of acetonitrile in a round bottom flask fitted with a stir bar and reflux condenser. The reaction was left to stir for 5 days at 40 °C. The compound was washed with 200 mL (10

x 20mL) of ethyl acetate and rotary evaporated. The resulting product was a pale yellow liquid (12.35 g, 90%, $C_7H_{16}N_2OBr$, Molar mass 221.10 g/mol). ^1H (400 MHz; DMSO-d_6) δ 3.08 (s, 3H), 3.67-3.70 (t, 2H), 3.88 (s, 3H), 4.37-4.39 (t, 2H), 7.49 (d, 1H), 8.00 (d, 1H), 9.24 (s, 1H) ^{13}C (101 MHz; DMSO-d_6) δ 36.2, 49.1, 58.5, 60.2, 70.1, 123.1, 123.9, 137.3.

16a. Synthesis of 1-(2-ethoxyethyl)-3-methylimidazolium bromide (EOEmim Br)

1-methylimidazole (5.00 g, 0.0609 mol) dissolved in 15 mL of acetonitrile in a round bottom flask fitted with a stir bar and reflux condenser was reacted with one equivalent of 2-bromoethylethylether (9.32 g, 0.0609 mol) dissolved in 15 mL of acetonitrile. The reaction mixture was left to stir for 4 days at 50 °C. The reaction mixture was rotary evaporated. The product was washed with 200 mL (10 x 20 mL) of ethyl acetate and rotary evaporated. The final product was a phase-separated mixture consisting of a yellow liquid, and a white solid with identical NMR spectra (12.87 g, 90%, $C_8H_{18}N_2OBr$, Molar mass 235.13 g/mol). ^1H (400 MHz; D_2O) δ 1.06-1.21 (t, 3H), 3.50-3.57 (m, 2H), 3.86 (s, 3H), 4.06-4.1 (t, 2H), 4.30-4.35 (t, 2H), 7.37 (d, 1H), 7.48 (d,1H), 8.71 (s, 1H) ^{13}C (101 MHz; D_2O) δ 13.1, 34.8, 35.1, 47.9, 48.1, 65.8, 66.8, 121.2, 121.5, 123.7.

17a. Synthesis of 1-(2-(2-methoxyethoxy)ethyl)-3-methylimidazolium bromide (EOEOMmim Br)

1-methylimidazole (2.24 g, 0.0273 mol) dissolved in 10 mL of acetonitrile in a round bottom flask fitted with a stir bar and reflux condenser was reacted with one equivalent of 1-bromo-2-(2-methoxyethoxy)ethane (5.00 g, 0.0273 mol) dissolved in 15 mL of acetonitrile, added drop wise with stirring. The reaction mixture was left to stir for 6 days at 45 °C. The resulting compound was washed with 200 mL (10 x 20 mL) of ethyl acetate and rotary evaporated. The final product was a pale yellow liquid (6.45 g, 89%, $C_9H_{20}N_2O_2Br$, Molar mass 265.15 g/mol). ^1H (400 MHz; D_2O) δ 3.39-3.41 (s, 3H), 3.64-3.69 (t, 2H), 3.71-3.79 (t, 2H), 3.90 (s, 3H), 3.93-3.98 (t, 2H), 4.42-4.48 (t, 2H), 7.49 (s, 1H), 7.59 (s, 1H), 8.79 (s, 1H); ^{13}C (101 MHz; D_2O) δ 35.78, 49.06, 58.07, 68.40, 69.49, 70.91, 122.52, 123.45, 136.19.

18a. Synthesis of 1-(2-(2-ethoxyethoxy)ethyl)-3-methylimidazolium bromide (EOEOEmim Br)

1-methylimidazole (2.50 g, 0.0304 mol) dissolved in 10 mL of acetonitrile in a round bottom flask fitted with a stir bar and reflux condenser was reacted with one equivalent of 2-(2-ethoxyethoxy)ethyl bromide (5.00 g, 0.0304 mol) dissolved in 15 mL of acetonitrile. The reaction mixture was left to stir for 7 days at 60 °C. The resulting compound was washed with 200 mL (10 x 20 mL) of ethyl acetate. The final product was a clear, colorless liquid (7.73 g, 91%, $C_{10}H_{22}N_2O_2$ Br, Molar mass 279.19 g/mol). ^1H (400 MHz; DMSO-d_6) δ 0.88-0.92 (t, 3H), 3.35-3.54 (m, 6H), 3.75-3.77 (t, 2H), 3.86 (s, 3H), 4.35-4.38 (t, 2H), 7.68 (d, 1H), 7.78 (d, 1H), 9.26 (s, 1H) ^{13}C (101 MHz; DMSO-d_6) δ 15.6, 36.2, 49.2, 65.9, 68.6, 69.4, 70.0, 123.1, 123.8, 137.3.

19a. Synthesis of 1-(2-(2-(2-methoxyethoxy)ethoxy)ethyl)-3-methylimidazolium bromide (EOEOEOMmim Br)

1-methylimidazole (4.12 g, 0.0502 mol) dissolved in 15 mL of acetonitrile in a round bottom flask fitted with a stir bar and reflux condenser was reacted with one equivalent of 1-(2-bromoethoxy)-2-(2-methoxyethoxy)ethane (11.41 g, 0.0502 mol) dissolved in 20 mL of acetonitrile. The reaction mixture was left to stir for 7 days at 60 °C. The resulting

compound was washed with 200 mL (10 x 20 mL) of ethyl acetate and then was rotary evaporated. The final product was a yellow liquid (13.50 g, 87%, $C_{11}H_{24}N_2O_3Br$, Molar mass 309.21 g/mol). ^{1}H (400 MHz; DMSO-d_6) δ 3.36 (s, 3H), 3.42-3.52 (m, 6H), 3.56-3.58 (t, 2H), 3.77-3.79 (t, 2H), 3.87 (s, 3H), 4.34-4.36 (t, 2H), 7.69 (s, 1H), 7.73 (s, 1H), 9.05 (s, 1H); ^{13}C(101 MHz; DMSO-d_6) δ 35.60, 48.69, 57.93, 68.05, 69.45, 69.47, 71.19, 122.65, 123.27, 136.75.

Preparation of Bis(trifluoromethylsulfonyl)amide (NTf_2) Ionic Liquids

1b. Synthesis of *N*-(2-methoxyethyl)-*N*-methyl pyrrolidinium bis(trifluoromethylsulfonyl)amide (EOM mPyrr NTf_2)

EOMmPyrr bromide (14.29 g, 0.064 mol) was reacted with one equivalent of lithium bis(trifluoromethylsulfonyl)amide (18.40 g, 0.064 mol) dissolved in 50 mL of distilled water. The reaction mixture was left to stir at room temperature for 24 hours. The product was washed with distilled water, until the wash tested negative for bromide with 50 mM aqueous silver nitrate. The product was then rotary evaporated and placed in a high vacuum oven at 60˚C for several days. The final product was a colorless liquid (18.52 g, 68%, Molar mass 424.38 g/mol, water content: 72 ppm). ^{1}H(400 MHz; DMSO-d_6) δ 3.74 (s, 2H), 3.55-3.57 (t, 2H), 3.49-3.51 (t, 4H), 3.31 (s, 3H), 3.02-3.05 (t, 3H), 2.09 (s, 4H); ^{13}C(101 MHz; DMSO-d_6) δ 124.74, 121.55, 118.35, 115.15, 66.42, 64.64, 62.54, 58.46, 48.40, 21.37, 21.26.

2b. Synthesis of *N*-(2-ethoxyethyl)-*N*-methyl pyrrolidinium bis(trifluoromethylsulfonyl)amide (EOEmPyrr NTf_2)

EOEmPyrr Br (10.62 g, 0.045 mol) was reacted with one equivalent of lithium bis(trifluoromethylsulfonyl)amide (12.81 g, 0.045 mol) dissolved in 50 mL of distilled water. The reaction mixture was left to stir at room temperature for a week. The resulting pale yellow liquid was washed with cold distilled water until the wash tested negative for bromide with 50 mM aqueous silver nitrate. The product was then rotary evaporated and dried in a high vacuum oven at 60 °C for several days to yield a pale yellow liquid (17.13 g, 87%, Molar mass 438.41 g/mol, water content: 77 ppm). ^{1}H(400 MHz; DMSO-d_6) δ 3.77-3.79 (t, 2H), 3.47-3.68 (m, 8H), 3.02 (s, 3H), 2.08 (s, 4H), 1.12-1.16 (t, 3H); ^{13}C(101 MHz; DMSO-d_6) δ 121.09, 117.89, 65.66, 64.19, 63.91, 62.18, 48.03, 20.90, 14.89.

3b. Synthesis of N-(2-methoxyethoxyethyl)-N-methyl pyrrolidinium bis(trifluoromethylsulfonyl)amide (EOEOMmPyrr NTf_2)

EOEOMmPyrr Br (13.14 g, 0.049 mol) was reacted with one equivalent of lithium bis(trifluoromethylsulfonyl)amide (14.06 g, 0.049 mol) dissolved in 50 mL of distilled water. The reaction mixture was left to stir at room temperature for 24 hours. The resulting dark brown viscous liquid was washed with cold distilled water until the wash tested negative for bromide with 50 mM aqueous silver nitrate. The product was then rotary evaporated and dried in a high vacuum oven at 60 °C for several days. The final product was a brown viscous liquid (7.52 g, 33%, Molar mass 468.48 g/mol, water content: 65 ppm). ^{1}H(400 MHz; DMSO-d_6) δ 3.84 (s, 2H), 3.55-3.60 (m, 4H), 3.46-3.52 (m, 6H), 3.26 (s, 3H), 3.03 (s, 3H), 2.09 (s, 4H); ^{13}C(101 MHz; DMSO-d_6) δ 124.74, 121.55,118.35, 115.15, 71.41, 69.81, 64.90, 64.70, 62.66, 58.33, 48.39, 21.21.

4b. Synthesis of *N*-(2-ethoxyethoxyethyl)-*N*-methyl pyrrolidinium bis(trifluoromethylsulfonyl)amide (EOEOEmPyrr NTf_2)

EOEOEmPyrr Br (16.66 g, 0.059 mol) was reacted with one equivalent of lithium bis(trifluoromethylsulfonyl)amide (16.94 g, 0.059 mol) dissolved in 50 mL of distilled water. The reaction mixture was left to stir at room temperature for 24 hours. The resulting liquid was washed with cold distilled water until the wash tested negative for bromide with 50 mM aqueous silver nitrate. The product was then rotary evaporated and dried in a high vacuum oven at 60 °C for several days. The final product was a pale yellow liquid (25.58 g, 90%, Molar mass 482.46 g/mol, water content: 79 ppm). ^{1}H(400 MHz; DMSO-d_6) δ 3.58-3.59 (t, 2H), 3.56-3.57 (t, 4H), 3.52-3.55 (t, 6H), 3.48-3.51 (q, 2H), 3.03 (s, 3H), 2.08 (s, 4H), 1.08-1.12 (t, 3H); ^{13}C(101 MHz; DMSO-d_6) δ 124.74, 121.55,118.35, 115.15, 69.53, 68.87, 65.48, 64.45, 64.16, 62.06, 49.01, 20.86, 15.09.

5b. Synthesis of *N*-methyl-*N*-(2-(2-(2-methoxyethoxy)ethoxy)ethyl)pyrrolidinium bis(trifluoromethylsulfonyl)amide (EOEOEOMmPyrr NTf_2)

EOEOEOMmPyrr Br (17.81 g, 0.0570 mol) was reacted with one equivalent of lithium bis(trifluoromethylsulfonyl)amide (16.37 g, 0.0570 mol) dissolved in 50 mL of distilled water. The reaction mixture was left to stir at room temperature for 24 hours. The resulting liquid was washed with cold distilled water and methylene chloride until the wash tested negative for bromide with 50 mM aqueous silver nitrate. The product was then rotary evaporated and dried in a high vacuum oven at 60 °C for several days. The final product was a pale yellow liquid (13.88 g, 48%, Molar mass 512.5 g/mol, water content: 22 ppm). ^{1}H(400 MHz; DMSO-d_6) δ 3.86 (s, 2H), 3.45-3.61 (m, 12H), 3.43-3.44 (t, 2H), 3.25 (s, 3H), 3.04 (s, 3H), 2.10 (s, 4H); ^{13}C(101 MHz; DMSO-d_6) δ 124.40, 121.20, 118.00, 114.80, 71.34, 69.56, 69.54, 69.52, 64.54, 64.40, 62.37, 57.98, 47.99, 20.88.

6b. Synthesis of *N*-methyl-*N*-pentylpyrrolidinium bis(trifluoromethylsulfonyl)amide (C_5mPyrr NTf_2)

C_5mPyrr Br (15.84 g, 0.067 mol) was reacted with one equivalent of lithium bis(trifluoromethylsulfonyl)amide (19.29 g, 0.067 mol) dissolved in 50 mL of distilled water. The reaction mixture was left to stir at room temperature for 24 hours. The resulting pale yellow liquid was washed with cold distilled water until the wash tested negative for bromide with 50 mM aqueous silver nitrate. The product was then rotary evaporated and dried in a high vacuum oven at 60 °C for several days to yield a pale yellow liquid (25.11 g, 86%, Molar mass 436.45 g/mol, water content 80 ppm). ^{1}H(400 MHz; DMSO-d_6) δ 3.37-3.46 (m, 4H), 3.25-3.30 (t, 2H), 2.98 (s, 3H), 2.09 (s, 2H), 1.67-1.74 (m, 2H), 1.30-1.37(m, 2H), 1.23-1.29 (m, 4H), 0.87-0.91 (t, 3H); ^{13}C(101 MHz; DMSO-d_6) δ 124.37, 121.17, 117.97, 114.78, 63.45, 47.53, 28.03, 25.57, 21.64, 21.09, 13.59, 13.55.

7b. Synthesis of *N*-heptyl-*N*-methylpyrrolidinium bis(trifluoromethylsulfonyl)amide (C_7mPyrr NTf_2)

C_7mPyrr Br (18.04 g, 0.068 mol) was reacted with one equivalent of lithium bis(trifluoromethylsulfonyl)amide (19.58 g, 0.068 mol) dissolved in 50 mL of distilled water. The reaction mixture was left to stir at room temperature for 24 hours. The resulting liquid was washed with cold distilled water until the wash tested negative for bromide with 50 mM aqueous silver nitrate. The product was then rotary evaporated and dried in a high vacuum oven at 60 °C for several days. The final product was a yellow liquid (17.13 g, 87%, Molar mass: 438.34 g/mol, water content: 112 ppm). ^{1}H(400 MHz; DMSO-d_6) δ 3.77-3.79 (t, 2H), 3.47-3.68 (m, 8H), 3.02 (s, 3H), 2.08 (s, 4H), 1.12-1.16 (t,

3H); ^{13}C(101 MHz; DMSO-d_6) δ 121.09, 117.89, 65.66, 64.19, 63.91, 62.18, 48.03, 20.90, 14.89.

8b. Synthesis of *N*-methyl-*N*-octylpyrrolidinium bis(trifluoromethylsulfonyl)amide (C_8mPyrr NTf_2)

C_8mpyrr Br (14.74 g, 0.05297 mol) was reacted with one equivalent of lithium bis(trifluoromethylsulfonyl)amide (15.21 g, 0.05297 mol) dissolved in 40 mL of distilled water. The reaction mixture was left to stir at room temperature for 24 hours. The resulting liquid was washed with cold distilled water until the wash tested negative for bromide with 50 mM aqueous silver nitrate. The product was then rotary evaporated. The resulting viscous liquid was dried in a high vacuum oven at 60 °C for several days. The final product was a yellow liquid (14.36 g, 57%, Molar mass 478.53 g/mol, water content: 95 ppm) ^{1}H(400 MHz; DMSO-d_6) δ 3.42-3.45 (t, 5H), 3.26-3.30 (t, 1H), 2.97 (s, 3H), 2.08 (s, 4H), 1.69 (s, 2H), 1.29 (s, 10H), 0.86-0.88 (t, 3H); ^{13}C(101 MHz; DMSO-d_6) δ 124.28, 121.07, 117.88, 114.68, 63.38, 63.11, 47.46, 31.13, 28.42, 25.87, 22.88, 21.99, 13.84.

9b. Synthesis of *N*-methyl-*N*-octylpyrrolidinium bis(trifluoromethylsulfonyl)amide (C_{10}mPyrr NTf_2)

C_{10}mpyrr Br (19.64 g, 0.0641 mol) was reacted with one equivalent of lithium bis(trifluoromethylsulfonyl)amide (18.37 g, 0.0641 mol) dissolved in 70 mL of distilled water. The reaction mixture was left to stir at room temperature for four days. The resulting liquid was washed with cold distilled water until the wash tested negative for bromide with 50 mM aqueous silver nitrate. The product was then rotary evaporated and dried in a high vacuum oven at 60 °C for several days. The final product was a yellow liquid (15.24 g, 47%, Molar mass 506.58 g/mol, water content 92 ppm). ^{1}H(400 MHz; DMSO-d_6) δ 0.83-0.87 (s, 3H), 1.25 (s, 14H), 1.67-1.68 (m, 2H), 2.07 (s, 4H), 2.96 (s, 3H), 3.24-3.29 (m, 2H), 3.40-3.44 (m, 4H); ^{13}C (101 MHz; DMSO-d_6) δ 14.37, 21.52, 22.55, 23.37, 26.37, 28.96, 29.11, 29.26, 29.35, 31.74, 47.92, 63.66, 63.85, 115.15, 118.35, 121.55, 124.75.

10b. Synthesis of 1-butyl-3-methylimidazolium bis(trifluoromethylsulfonyl)amide (C_4mim NTf_2)

C_4mim Br (10.00g, 0.04569 mol) was reacted with one equivalent of lithium bis(trifluoromethylsulfonyl)amide (13.12 g, 0.04569 mol) dissolved in 40 mL of distilled water. The reaction mixture was stirred at room temperature for one day. The resulting colorless liquid was washed with cold distilled water until the wash tested negative for bromide with 50 mM aqueous silver nitrate. The product was then rotary evaporated and dried in a high vacuum oven at 60 °C for several days. The final product was a clear, colorless liquid (16.09 g, 84%, 419.46 g/mol, water content: 97 ppm). ^{1}H (400 MHz; DMSO-d_6) δ 0.85-0.89 (t, 3H), 1.22-1.32 (m, 2H), 1.76-1.85 (m, 2H), 3.85 (s, 3H), 7.39 (d, 1H), 7.44-7.45 (d, 1H); ^{13}C (101 MHz; DMSO-d_6) δ 12.7, 18.6, 31.3. 35.8, 49.3, 114.6, 117.8, 121.0, 122.4, 124.2, 127.5, 135.6.

11b. Synthesis of 1-methyl-3-pentylimidazolium bis(trifluoromethylsulfonyl)amide (C_5mim NTf_2)

C_5mim Br (15.02 g, 0.06451 mol) was reacted with one equivalent of lithium bis(trifluoromethylsulfonyl)amide (18.54 g, 0.06451 mol) dissolved in 40 mL of distilled water. The reaction mixture was stirred at room temperature for 1 day. The resulting

colorless liquid was washed with cold distilled water until the wash tested negative for bromide with 50 mM aqueous silver nitrate. The product was then rotary evaporated and dried in a high vacuum oven at 60 °C for several days. The final product was a clear, colorless liquid (17.01 g, 61%, 433.51 g/mol, water content: 90 ppm). ^{1}H (400 MHz; DMSO-d_6) δ 0.75-0.79 (t, 3H), 1.17-1.24 (m, 4H), 1.75-1.81 (m, 2H), 3.80 (s, 3H), 4.08-4.11 (t, 2H), 7.33-7.34 (d, 1H), 7.38 (d, 1H) ^{13}C (101 MHz; DMSO-d_6) δ 12.2, 20.4, 27.9, 34.7, 48.6, 114.6, 117.8, 121.0, 121.2, 122.4, 124.2, 134.6.

12b. Synthesis of 1-heptyl-3-methylimidazolium bis(trifluoromethylsulfonyl)amide (C_7mim NTf_2)

C_7mim Br (16.09 g, 0.06162 mol) was reacted with one equivalent of lithium bis(trifluoromethylsulfonyl)amide (17.69 g, 0.06162 mol) dissolved in 40 mL of distilled water. The reaction mixture was stirred at room temperature for one day. The resulting colorless liquid was washed with cold distilled water until the wash tested negative for bromide with 50 mM aqueous silver nitrate. The product was then rotary evaporated and dried in a high vacuum oven at 60 °C for several days. The final product was a clear, colorless liquid (16.94 g, 62%, 461.44 g/mol, water content: 93 ppm). ^{1}H (400 MHz; DMSO-d_6) δ 0.87 (t, 3H), 1.01-1.04 (m, 2H), 1.13-1.26 (m, 6H), 1.73-1.81 (m, 2H), 3.88 (s, 3H), 4.17-4.21 (t, 2H), 7.78 (d, 1H), 7.86 (d, 1H), 9.36 (s, 1H) ^{13}C (101 MHz; DMSO-d_6) δ 14.3, 21.2, 25.9, 28.5, 29.9, 31.5, 36.2, 49.2, 114.6, 117.8, 121.0, 122.7, 123.9, 124.2, 137.0.

13b. Synthesis of 1-methyl-3-octylimidazolium bis(trifluoromethylsulfonyl)amide (C_8mim NTf_2)

C_8mim Br (16.79 g, 0.06102 mol) was reacted with one equivalent of lithium bis(trifluoromethylsulfonyl)amide (17.52 g, 0.06102 mol) dissolved in 40 mL of distilled water. The reaction mixture was stirred at room temperature for one day. The resulting colorless liquid was washed with cold distilled water until the wash tested negative for bromide with 50 mM aqueous silver nitrate. The product was then rotary evaporated and dried in a high vacuum oven at 60 °C for several days. The final product was a clear, colorless liquid (22.62 g, 77%, 475.31 g/mol, water content: 93 ppm). ^{1}H (400 MHz; DMSO-d_6) δ 0.87 (t, 3H), 1.01-1.04 (m, 2H), 1.13-1.26 (m, 6H), 1.73-1.81 (m, 2H), 1.84-1.87 (m, 2H), 3.88 (s, 3H), 4.17-4.21 (t, 2H), 7.78 (d, 1H), 7.86 (d, 1H), 9.36 (s, 1H) ^{13}C (101 MHz; DMSO-d_6) δ 14.3, 21.2, 25.9, 28.5, 27.6, 29.9, 31.5, 36.2, 49.2, 114.6, 117.8, 121.0, 122.7, 123.9, 124.2, 137.0.

14b. Synthesis of 1-decyl-3-methylimidazolium bis(trifluoromethylsulfonyl)amide (C_{10}mim NTf_2)

C_{10}mim Br (5.83 g, 0.01922 mol) was reacted with one equivalent of lithium bis(trifluoromethylsulfonyl)amide (5.52 g, 0.01922 mol) dissolved in 40 mL of distilled water. The reaction mixture was stirred at room temperature for one day. The resulting colorless liquid was washed with cold distilled water until the wash tested negative for bromide with 50 mM aqueous silver nitrate. The product was then rotary evaporated and dried in a high vacuum oven at 60 °C for several days. The final product was a clear, colorless liquid (9.50 g, 98%, 503.55 g/mol, water content: 249 ppm). ^{1}H(400 MHz; DMSO-d_6) δ 0.83-0.86 (t, 3H), 1.24 (s, 14H), 1.76-1.79 (m, 2H), 3.84 (s, 3H), 4.12-4.16 (t, 2H), 7.67 (s, 1H), 7.74 (s, 1H), 9.08 (s, 1H); ^{13}C (101 MHz; DMSO-d_6) δ 13.83, 22.08, 25.49, 28.37, 28.67, 28.82, 28.90, 29.39, 31.29, 35.69, 48.81, 114.71, 117.91, 121.11, 122.24, 123.58, 124.31, 136.49.

15b. Synthesis of 1-(2-ethoxymethyl)-3-methylimidazolium bis(trifluoromethylsulfonyl)-amide (EOMmim NTf_2)

EOMmim Br (13.35 g, 0.06042 mol) was reacted with one equivalent of lithium bis(trifluoromethylsulfonyl)amide (17.35 g, 0.06042 mol) dissolved in 40 mL of distilled water. The reaction mixture was stirred at room temperature for one day. The resulting colorless liquid was washed with cold distilled water until the wash tested negative for bromide with 50 mM aqueous silver nitrate. The product was then rotary evaporated and dried in a high vacuum oven at 60 °C for several days. The final product was a clear, colorless liquid (13.39 g, 53%, 421.33 g/mol, water content: 91 ppm). ^{1}H (400 MHz; DMSO-d_6) δ 3.08 (s, 3H), 3.67-3.70 (t, 2H), 3.88 (s, 3H), 4.37-4.39 (t, 2H), 7.49 (d, 1H), 8.00 (d, 1H), 9.24 (s, 1H), ^{13}C (101 MHz; DMSO-d_6) δ 36.2, 49.1, 58.5, 60.2, 70.1, 114.6, 117.8, 121.0, 123.1, 123.9, 124.2, 137.3.

16b. Synthesis of 1-(2-ethoxyethyl)-3-methylimidazolium bis(trifluoromethylsulfonyl)-amide (EOEmim NTf_2)

EOEmim Br (14.90 g, 0.06324 mol) was reacted with one equivalent of lithium bis(trifluoromethylsulfonyl)amide (18.21 g, 0.06324 mol) dissolved in 40 mL of distilled water. The reaction mixture was stirred at room temperature for one day. The resulting colorless liquid was washed with cold distilled water until the wash tested negative for bromide with 50 mM aqueous silver nitrate. The product was then rotary evaporated and dried in a high vacuum oven at 60 °C for several days. The final product was a clear, colorless liquid (16.94 g, 62%, 435.38 g/mol, water content: 90 ppm). ^{1}H (400 MHz; DMSO-d_6) δ 1.06-1.21 (t, 3H), 3.50-3.57 (m, 2H), 3.86 (s, 3H), 4.06-4.1 (t, 2H), 4.30-4.35 (t, 2H), 7.37 (d, 1H), 7.48 (d,1H), 8.71 (s, 1H) ^{13}C (101 MHz; DMSO-d_6) δ 13.1, 34.8, 35.1, 47.9, 48.1, 65.8, 66.8, 114.6, 117.8, 121.0, 121.2, 121.5, 123.7, 124.2.

17b. Synthesis of 1-(2-(2-methoxyethoxy)ethyl)-3-methylimidazolium bis(trifluoro-methylsulfonyl)amide (EOEOMmim NTf_2)

EOEOMmim Br (6.45 g, 0.02432 mol) was reacted with one equivalent of lithium bis(trifluoromethylsulfonyl)amide (6.98 g, 0.02432 mol) dissolved in 40 mL of distilled water. The reaction mixture was stirred at room temperature for one day. The resulting colorless liquid was washed with cold distilled water until the wash tested negative for bromide with 50 mM aqueous silver nitrate. The product was then rotary evaporated and dried in a high vacuum oven at 60 °C for several days. The final product was a clear, colorless liquid (8.23 g, 73%, 465.38 g/mol, water content: 88 ppm). ^{1}H (400 MHz; DMSO-d_6) δ 3.39-3.41 (s, 3H), 3.64-3.69 (t, 2H), 3.71-3.79 (t, 2H), 3.90 (s, 3H), 3.93-3.98 (t, 2H), 4.42-4.48 (t, 2H), 7.49 (s, 1H), 7.59 (s, 1H), 8.79 (s, 1H); ^{13}C (101 MHz; DMSO-d_6) δ 35.78, 49.06, 58.07, 68.40, 69.49, 70.91, 114.6, 117.8, 121.0, 122.52, 123.45, 124.2, 136.19.

18b. Synthesis of 1-(2-(2-ethoxyethoxy)ethyl)-3-methylimidazolium bis(trifluoro-methylsulfonyl)amide (EOEOEmim NTf_2)

EOEOEmim Br (7.73 g, 0.02773 mol) was reacted with one equivalent of lithium bis(trifluoromethylsulfonyl)amide (7.96 g, 0.02773 mol) dissolved in 40 mL of distilled water. The reaction mixture was stirred at room temperature for one day. The resulting colorless liquid was washed with cold distilled water until the wash tested negative for bromide with 50 mM aqueous silver nitrate. The product was then rotary evaporated and dried in a high vacuum oven at 60 °C for several days. The final product was a clear,

colorless liquid (7.13 g, 54 %, 479.41 g/mol, water content: 94 ppm). ^{1}H (400 MHz; DMSO-d_6) δ 0.88-0.92 (t, 3H), 3.35-3.54 (m, 6H), 3.75-3.77 (t, 2H), 3.86 (s, 3H), 4.35-4.38 (t, 2H), 7.68 (d, 1H), 7.78 (d, 1H), 9.26 (s, 1H) ^{13}C (101 MHz; DMSO-d_6) δ 15.6, 36.2, 49.2, 65.9, 68.6, 69.4, 70.0, 114.6, 117.8, 121.0, 123.1, 123.8, 124.2, 137.3.

19b. Synthesis of 1-(2-(2-(2-methoxyethoxy)ethoxy)ethyl)-3-methylimidazolium bis(trifluoromethylsulfonyl)amide (EOEOEOMmim NTf_2)

EOEOEOMmim Br (15.50 g, 0.05014 mol) was reacted with one equivalent of lithium bis(trifluoromethylsulfonyl)amide (14.38 g, 0.05014 mol) dissolved in 40 mL of distilled water. The reaction mixture was stirred at room temperature for one day. The resulting colorless liquid was washed with cold distilled water until the wash tested negative for bromide with 50 mM aqueous silver nitrate. The product was then rotary evaporated and dried in a high vacuum oven at 60 °C for several days. The final product was a clear, colorless liquid (21.22 g, 83%, 509.44 g/mol, water content: 95 ppm). ^{1}H (400 MHz; DMSO-d_6) δ 3.36 (s, 3H), 3.42-3.52 (m, 6H), 3.56-3.58 (t, 2H), 3.77-3.79 (t, 2H), 3.87 (s, 3H), 4.34-4.36 (t, 2H), 7.69 (s, 1H), 7.73 (s, 1H), 9.05 (s, 1H); ^{13}C(101 MHz; DMSO-d_6) δ 35.60, 48.69, 57.93, 68.05, 69.45, 69.47, 71.19, 114.6, 117.8, 121.0, 122.65, 123.27, 124.2, 136.75.

Physical Measurements: Water contents of the ionic liquid samples were determined using a Mettler Toledo DL39 coulometric Karl Fischer titrator connected to an analytical balance. The water contents of the samples used for the property measurements ranged from 22-249 ppm.

Viscosities were measured with a Cambridge Applied Systems ViscoLab 4100 electromagnetic reciprocating piston viscometer that was temperature regulated by a Lauda RM-6 circulating bath with a 70/30 v/v propylene glycol/water mixture. The viscometer was calibrated with S600S viscosity reference standard from Koehler Instrument Company (Bohemia, NY). The viscometer was housed in a moisture controlled dry box with an active N_2 purge during data acquisition. The dry box was fitted with a hygrometer and measurements were made when the moisture level was less than 1%. Viscosities for each IL were recorded at intervals between 9 ˚C and 90 ˚C in ascending and descending order within their liquid ranges. The data were then fit using the logarithmic form of the Vogel-Tammann-Fulcher relation, $\ln(\eta(T)) = \ln(\eta_0) + [DT_0/(T - T_0)]$, in order to obtain better fitting of points in the low-viscosity range. Each data set included a value of 1×10^{13} cP at the liquid's glass transition temperature T_g, according to the practice of Angell,[38] which leads to more consistent trends across a set of liquids. Values of $\ln(\eta_0)$, D and T_0 are given in Table II. Where indicated, viscosity data for the VTF fit were taken from the literature, however, all VTF parameters shown are the results of our own fits since the literature fits seldom include a data point at T_g.

Thermal profiles: A TA Instruments Q100 Differential Scanning Calorimeter (DSC) was used to determine onset temperatures for melting points and glass transitions (T_g). Scan rates were 5 ˚C/min. The data were analyzed using TA Universal Analysis 2000 software.

Variable temperature ionic conductivities: Two instruments were used over the course of this work. Conductivities of C_4mPyrr, C_5mPyrr, EOMmPyrr, EOEmPyrr and C_8mim NTf_2 were measured by complex impedance measurements using a computer-controlled Hewlett-Packard 4129A Impedance Analyzer in the frequency range from 5 Hz to 10

MHz. The samples were placed into a homemade cell consisting of a scintillation vial with electrodes inserted through the cap. The cell constant was determined using an aqueous 0.053% KCl calibration solution (YSI 3167, 1000 ± 10 μS cm^{-1} at 25 °C, Yellow Springs Instruments). All other measurements were performed with a YSI model 3200 Conductivity Instrument fitted with a YSI model 3253 probe, housed in the moisture control dry box used for the viscosity measurements.

X-ray scattering studies: The X-ray scattering experiments were done at beamline 11-ID-B of the Advanced Photon Source as described in detail recently.[2,49,57,58] The IL samples were contained in flame-sealed 3 mm glass NMR tubes under argon atmosphere. The X-ray beam wavelength was 0.21140 Å. The 2-D X-ray scattering pattern is recorded using a Perkin-Elmer amorphous silicon 2D area detector. The sample temperature was controlled at 25 ˚C. Each sample was exposed to the X-ray beam for 5 minutes. The sample-to-detector distance was approximately 21.0 cm and was calibrated using a sample of powdered CeO_2. The 2D scattering pattern was integrated from center to edge using Fit2D software[62] to obtain the scattering intensity *I(q)* vs. the scattering vector $q = (4\pi/\lambda)\sin(\theta)$, over a range of $0.2 < q < 20$ 1/Å. The X-ray structure factor $S(q)$ is calculated from *I(q)* using PDFgetX2 software.[63]

Molecular dynamics (MD) simulations: Molecular dynamics simulations on EOEOEOMmPyrr NTf_2 and EOEOEOMmim NTf_2 were run using the GROMACS 2016.1 package with CPU acceleration.[64-66] Each simulation box with periodic boundary conditions contained 1,000 ion pairs. The boxes are equilibrated using the following protocol under 1 bar and 298 K: The box was initialized during a 50 ps simulation where all the atoms have a 10% fraction charge of the defined values. Berendsen pressure and temperature coupling were applied.[66] Next, the temperature coupling method was changed to V-rescale[67] for another 200 ps. Then the charges of all atoms were scaled to 50% of full charge and the box was equilibrated for 500 ps. Finally, full charges were applied to the atoms and the system was equilibrated using V-rescale temperature coupling and Berendsen pressure coupling for 2 ns. Next, a Nosé-Hoover thermostat[68,69] and a Parrinello-Rahman barostat[70] were applied to equilibrate the system for another 10 ns. The final production run was done for 2 ns with coordinates saved every 1 ps to calculate g(r) and S(q). During the equilibration and final production run, the equations of motion were integrated using the leapfrog algorithm with a time step of 1 fs, the default parameter in GROMACS.[64,65] We also used the default Verlet cutoff scheme in GROMACS,[64,65] with neighboring list radii and cutoffs for Coulomb and Lennard-Jones interactions all set to 1.5 nm. Long-range electrostatic potentials were calculated using the Particle Mesh Ewald (PME) summation method[71,72] with an interpolation order of 6 and a FFT grid spacing of 0.08 nm in a 3D periodic geometry. We used the Canongia Lopes and Pádua (CL&P) force field[73-76] together with the optimized potential for liquid simulations: all-atom (OPLS-AA) force field[77] for the simulations to obtain the best match with structural data. The CL&P transferable force field for ILs, in itself a generalization of Jorgensen's OPLS-AA force field, has provided very good predictive capability for IL structures.[2,49,53,56-58] The radial pair distribution functions $g(r)$ between all atom pairs are obtained from the trajectory of the production run. The structure functions are calculated using Equation 2:

$$S(q) = \frac{\rho_0 \sum_i \sum_j x_i x_j f_i(q) f_j(q) \int_0^\infty 4\pi r^2 (g_{ij}(r) - 1) \frac{sin(qr)}{qr} W(r) dr}{[\sum_i^n x_i f_i(q)]^2} \quad (2)$$

where ρ_0 is the number density of the box, $g_{ij}(r)$ is the radial distribution function between atom type *i* and atom type *j*, respectively, x_i and $f_i(q)$ are the mole fraction and atomic form factor of atom type *i*, respectively, and $W(r) = \sin(2\pi r/L)/(2\pi r/L)$ is the Lorch function. The densities calculated for EOEOEOMmPyrr NTf_2 and EOEOEOMmim NTf_2 were 1.364 and 1.441 g cm^{-3} respectively. Radial and spatial distribution functions and other molecular graphics were created with the TRAVIS 1.14.0[29] and VMD 1.9.3[78] software packages.

Acknowledgments

The authors thank the National Institutes of Health (NIH), Bridges to the Baccalaureate Program: Research Initiative for Minority Students (RIMS) at Queensborough Community College of the City University of New York and the Office of Educational Programs at Brookhaven National Laboratory for student internship support. SL-R, EWC, and NZ (from June 2015) were supported by the National Science Foundation Grant CHE-1362272 (Rutgers). The authors thank Dr. Alison Funston, Dr. Tomasz Szreder, Dr. Marie Thomas, Kijana Kerr, Jasmine Hatcher and Sharon Ramati for some of the physical parameter measurements on the pyrrolidinium compounds and Xing Li for synthesizing some of the alkylimidazolium bromides. JFW, SBD and NZ (up to May 2015) and the IL physical characterization work at BNL were supported by the U.S. Department of Energy, Office of Science, Office of Workforce Development for Teachers and Scientists (WDTS) under the Community College Internships Program (CCI), and by the Office of Basic Energy Sciences, Division of Chemical Sciences, Geosciences and Biosciences, under contracts DE-AC02-98CH10886 and DE-SC0012704. This research used resources of the Advanced Photon Source, a U.S. Department of Energy (DOE) Office of Science User Facility operated for the DOE Office of Science by Argonne National Laboratory under Contract No. DE-AC02-06CH11357. We thank APS beamline scientists, Dr. Olaf J. Borkiewicz, Kevin A. Beyer and Dr. Karena W. Chapman for their assistance in X-ray data collection.

References

1. K. Shimizu, C. E. S. Bernardes, A. Triolo and J. N. C. Lopes, *Phys. Chem. Chem. Phys.*, **15**, 16256 (2013).
2. H. K. Kashyap, C. S. Santos, R. P. Daly, J. J. Hettige, N. S. Murthy, H. Shirota, E. W. Castner and C. J. Margulis, *J. Phys. Chem. B*, **117**, 1130 (2013).
3. R. Hayes, G. G. Warr and R. Atkin, *Chem. Rev.*, **115**, 6357 (2015).
4. H. Shirota, H. Fukazawa, T. Fujisawa and J. F. Wishart, *J. Phys. Chem. B*, **114**, 9400 (2010).
5. H. Y. Lee, H. Shirota and E. W. Castner, *J. Phys. Chem. Lett.*, **4**, 1477 (2013).
6. M. Furlani, I. Albinsson, B. E. Mellander, G. B. Appetecchi and S. Passerini, *Electrochim. Acta*, **57**, 220 (2011).
7. S. K. Tang, G. A. Baker and H. Zhao, *Chem. Soc. Rev.*, **41**, 4030 (2012).
8. E. I. Cooper and C. A. Angell, *Solid State Ionics*, **9-10**, 617 (1983).

9. Z. B. Zhou, H. Matsumoto and K. Tatsumi, *Chem. Eur. J.*, **11**, 752 (2005).
10. Y. D. Jin, S. H. Fang, L. Yang, S. I. Hirano and K. Tachibana, *J. Power Sources*, **196**, 10658 (2011).
11. S. Fang, Y. Jin, L. Yang, S. Hirano, K. Tachibana and S. Katayama, *Electrochim. Acta*, **56**, 4663 (2011).
12. S. P. Luo, S. A. Zhang, Y. F. Wang, A. B. Xia, G. C. Zhang, X. H. Du and D. Q. Xu, *J. Org. Chem.*, **75**, 1888 (2010).
13. L. Carbone, M. Gobet, J. Peng, M. Devany, B. Scrosati, S. Greenbaum and J. Hassoun, *ACS Appl. Mater. Interfaces*, **7**, 13859 (2015).
14. T. Sato, G. Masuda and K. Takagi, *Electrochim. Acta*, **49**, 3603 (2004).
15. M. Wang, X. R. Xiao, X. W. Zhou, X. P. Li and Y. Lin, *Sol. Energy Mater. Sol. Cells*, **91**, 785 (2007).
16. P. Sharma, S. H. Choi, S. D. Park, I. H. Baek and G. S. Lee, *Chem. Eng. J.*, **181**, 834 (2012).
17. M. Kanakubo, T. Makino, T. Taniguchi, T. Nokami and T. Itoh, *ACS Sustain. Chem. Eng.*, **4**, 525 (2016).
18. Y. Zhao, J. Y. Wang, H. C. Jiang and Y. Q. Hu, *Energy Fuels*, **29**, 1941 (2015).
19. J. Wang, S. J. Zeng, L. Bai, H. S. Gao, X. P. Zhang and S. J. Zhang, *Ind. Eng. Chem. Res.*, **53**, 16832 (2014).
20. L. C. Branco, J. N. Rosa, J. J. M. Ramos and C. A. M. Afonso, *Chem. Eur. J.*, **8**, 3671 (2002).
21. J. D. Holbrey, A. E. Visser, S. K. Spear, W. M. Reichert, R. P. Swatloski, G. A. Broker and R. D. Rogers, *Green Chem.*, **5**, 129 (2003).
22. N. Kimizuka and T. Nakashima, *Langmuir*, **17**, 6759 (2001).
23. S. Park and R. J. Kazlauskas, *J. Org. Chem.*, **66**, 8395 (2001).
24. Z. J. Wang, Y. C. Pei, J. Zhao, Z. Y. Li, Y. J. Chen and K. L. Zhuo, *J. Phys. Chem. B*, **119**, 4471 (2015).
25. J. Pernak, A. Czepukowicz and R. Pozniak, *Ind. Eng. Chem. Res.*, **40**, 2379 (2001).
26. J. Pernak, K. Sobaszkiewicz and I. Mirska, *Green Chem.*, **5**, 52 (2003).
27. M. Matsumoto, Y. Saito, C. Park, T. Fukushima and T. Aida, *Nat. Chem.*, **7**, 730 (2015).
28. G. D. Smith, O. Borodin, L. Y. Li, H. Kim, Q. Liu, J. E. Bara, D. L. Gin and R. Nobel, *Phys. Chem. Chem. Phys.*, **10**, 6301 (2008).
29. M. Brehm and B. Kirchner, *J. Chem. Inf. Model.*, **51**, 2007 (2011).
30. H. Jin, B. O'Hare, J. Dong, S. Arzhantsev, G. A. Baker, J. F. Wishart, A. J. Benesi and M. Maroncelli, *J. Phys. Chem. B*, **112**, 81 (2008).
31. S. J. Zhang, N. Sun, X. Z. He, X. M. Lu and X. P. Zhang, *J. Phys. Chem. Ref. Data*, **35**, 1475 (2006).
32. T. J. Hughes, T. Syed, B. F. Graham, K. N. Marsh and E. F. May, *J. Chem. Eng. Data*, **56**, 2153 (2011).
33. A. M. Funston and J. F. Wishart, in *Ionic Liquids IIIA: Fundamentals, Progress, Challenges, and Opportunities, Properties and Structure*, R. D. Rogers and K. R. Seddon, Eds.; Vol. 901, p. 102, Amer Chemical Soc: Washington, (2005).
34. A. M. Funston, T. A. Fadeeva, J. F. Wishart and E. W. Castner, *J. Phys. Chem. B*, **111**, 4963 (2007).
35. M. Dobbelin, I. Azcune, M. Bedu, A. R. de Luzuriaga, A. Genua, V. Jovanovski, G. Cabanero and I. Odriozola, *Chem. Mat.*, **24**, 1583 (2012).

36. M. Tariq, P. J. Carvalho, J. A. P. Coutinho, I. M. Marrucho, J. N. C. Lopes and L. P. N. Rebelo, *Fluid Phase Equilib.*, **301**, 22 (2011).
37. R. Bini, M. Malvaldi, W. R. Pitner and C. Chiappe, *J. Phys. Org. Chem.*, **21**, 622 (2008).
38. W. Xu, E. I. Cooper and C. A. Angell, *J. Phys. Chem. B*, **107**, 6170 (2003).
39. Z. F. Fei, W. H. Ang, D. B. Zhao, R. Scopelliti, E. E. Zvereva, S. A. Katsyuba and P. J. Dyson, *J. Phys. Chem. B*, **111**, 10095 (2007).
40. O. Russina and A. Triolo, *Faraday Discuss.*, **154**, 97 (2012).
41. A. Triolo, O. Russina, R. Caminiti, H. Shirota, H. Y. Lee, C. S. Santos, N. S. Murthy and E. W. Castner, *Chem. Commun.*, **48**, 4959 (2012).
42. J. N. Canongia Lopes and A. A. H. Padua, *J. Phys. Chem. B*, **110**, 3330 (2006).
43. K. Shimizu, M. F. Costa Gomes, A. A. H. Padua, L. P. N. Rebelo and J. N. C. Lopes, *Theochem-J. Mol. Struct.*, **946**, 70 (2010).
44. K. Shimizu, C. E. S. Bernardes and J. N. Canongia Lopes, *J. Phys. Chem. B*, **118**, 567 (2014).
45. A. Triolo, O. Russina, H. J. Bleif and E. Di Cola, *J. Phys. Chem. B*, **111**, 4641 (2007).
46. O. Russina, A. Triolo, L. Gontrani and R. Caminiti, *J. Phys. Chem. Lett.*, **3**, 27 (2012).
47. C. S. Santos, N. S. Murthy, G. A. Baker and E. W. Castner, *J. Chem. Phys.*, **134**, 121101 (2011).
48. S. Li, J. L. Banuelos, J. Guo, L. Anovitz, G. Rother, R. W. Shaw, P. C. Hillesheim, S. Dai, G. A. Baker and P. T. Cummings, *J. Phys. Chem. Lett.*, **3**, 125 (2012).
49. H. K. Kashyap, C. S. Santos, N. S. Murthy, J. J. Hettige, K. Kerr, S. Ramati, J. Gwon, M. Gohdo, S. I. Lall-Ramnarine, J. F. Wishart, C. J. Margulis and E. W. Castner, *J. Phys. Chem. B*, **117**, 15328 (2013).
50. S. M. Urahata and M. C. C. Ribeiro, *J. Chem. Phys.*, **120**, 1855 (2004).
51. Y. T. Wang and G. A. Voth, *J. Am. Chem. Soc.*, **127**, 12192 (2005).
52. H. V. R. Annapureddy, H. K. Kashyap, P. M. De Biase and C. J. Margulis, *J. Phys. Chem. B*, **114**, 16838 (2010).
53. H. K. Kashyap, J. J. Hettige, H. V. R. Annapureddy and C. J. Margulis, *Chem. Commun.*, **48**, 5103 (2012).
54. J. J. Hettige, H. K. Kashyap, H. V. R. Annapureddy and C. J. Margulis, *J. Phys. Chem. Lett.*, **4**, 105 (2013).
55. A. Kaintz, G. Baker, A. Benesi and M. Maroncelli, *J. Phys. Chem. B*, **117**, 11697 (2013).
56. C. S. Santos, H. V. R. Annapureddy, N. S. Murthy, H. K. Kashyap, E. W. Castner, Jr. and C. J. Margulis, *J. Chem. Phys.*, **134**, 064501 (2011).
57. B. Wu, H. Shirota, S. Lall-Ramnarine and E. W. Castner, *J. Chem. Phys.*, **145**, 114501 (2016).
58. B. Wu, Y. Yamashita, T. Endo, K. Takahashi and E. W. Castner, *J. Chem. Phys.*, **145**, 244506 (2016).
59. O. Russina, A. Triolo, L. Gontrani, R. Caminiti, D. Xiao, L. G. Hines, R. A. Bartsch, E. L. Quitevis, N. Pleckhova and K. R. Seddon, *J. Phys.-Condens. Matter*, **21**, 424121 (2009).
60. A. Luzar and D. Chandler, *Phys. Rev. Lett.*, **76**, 928 (1996).
61. D. H. Zaitsau, A. V. Yermalayeu, S. P. Verevkin, J. E. Bara and A. D. Stanton, *Ind. Eng. Chem. Res.*, **52**, 16615 (2013).

62. A. Hammersley, S. Svensson, M. Hanfland, A. Fitch and D. Hausermann, *High Pressure Res.*, **14**, 235 (1996).
63. X. Qiu, J. W. Thompson and S. J. L. Billinge, *J. Appl. Crystallogr.*, **37**, 678 (2004).
64. M. J. Abraham, T. Murtola, R. Schulz, S. Pall, J. C. Smith, B. Hess and E. Lindahl, *SoftwareX*, **1-2**, 19 (2015).
65. S. Pronk, S. Páll, R. Schulz, P. Larsson, P. Bjelkmar, R. Apostolov, M. R. Shirts, J. C. Smith, P. M. Kasson, D. van der Spoel, B. Hess and E. Lindahl, *Bioinformatics*, **29**, 845 (2013).
66. H. J. C. Berendsen, D. van der Spoel and R. van Drunen, *Comput. Phys. Commun.*, **91**, 43 (1995).
67. G. Bussi, D. Donadio and M. Parrinello, *J. Chem. Phys.*, **126**, 014101 (2007).
68. S. Nosé, *J. Chem. Phys.*, **81**, 511 (1984).
69. S. Nosé, *Mol. Phys.*, **52**, 255 (1984).
70. M. Parrinello and A. Rahman, *J. Appl. Phys.*, **52**, 7182 (1981).
71. T. Darden, D. York and L. Pedersen, *J. Chem. Phys.*, **98**, 10089 (1993).
72. U. Essmann, L. Perera, M. L. Berkowitz, T. Darden, H. Lee and L. G. Pedersen, *J. Chem. Phys.*, **103**, 8577 (1995).
73. J. N. Canongia Lopes and A. A. H. Padua, *Theor. Chem. Acc.*, **131**, 1129 (2012).
74. J. N. Canongia Lopes, J. Deschamps and A. A. H. Padua, *J. Phys. Chem. B*, **108**, 2038 (2004).
75. J. N. Canongia Lopes and A. A. H. Padua, *J. Phys. Chem. B*, **108**, 16893 (2004).
76. J. N. Canongia Lopes and A. A. H. Padua, *J. Phys. Chem. B*, **110**, 19586 (2006).
77. R. C. Rizzo and W. L. Jorgensen, *J. Am. Chem Soc.*, **121**, 4827 (1999).
78. W. Humphrey, A. Dalke and K. Schulten, *J. Mol. Graphics*, **14**, 33 (1996).